SUPPORTING INFORMATION

Advances of photon avalanche luminescence in inorganic lanthanide doped nanomaterials

Marcin Szalkowski[a,b], Agata Kotulska[a], Magdalena Dudek[a], Zuzanna Korczak[a], Martyna Majak[a], Lukasz Marciniak[a], Malgorzata Misiak[a], Katarzyna Prorok[a], Artiom Skripka[c,d], James Schuck[e], Emory Chan[c]*, Artur Bednarkiewicz[a]*

a. Institute of Low Temperature and Structure Research, Polish Academy of Sciences, ul.Okolna 2, 50-422 Wroclaw, Poland
b. Nanophotonics Group, Institute of Physics, Faculty of Physics, Astronomy and Informatics, Nicolaus Copernicus University in Toruń, 87-100 Toruń, ul. Grudziądzka 5, Poland
c. Department of Chemistry, Oregon State University, Corvallis, Oregon 97331, United States
d. Department of Mechanical Engineering, Columbia University, New York, NY, United States
e. The Molecular Foundry, Lawrence Berkeley National Laboratory, Berkeley, California 94720, United States

1 Overview of photon avalanche in lanthanide doped materials

In this chapter, the photon avalanche phenomenon is reviewed and discussed for every single lanthanide ion (among those, where PA and PA-like mechanisms are expected). Not only historical achievements, but also already experimentally confirmed as well as hypothetically predicted PA or PA-like emissions are briefly discussed and commented. PA emission in bulk and fiber PA materials were reviewed previously [1–3]. The convention we assumed presents energy levels with optical transitions being important for achieving the PA emission, starting from various ESA processes, various CR looping mechanisms, non-radiative quenching and various possible emission transitions, all of them accompanied by transition wavelengths (expressed in nm) and electron dipole lines strengths:

$$A_{ij} = \sum_{\lambda=2,4,6} \Omega_\lambda \cdot \left|\left\langle 4f^N\alpha[SL]J \middle\| U^{(\lambda)} \middle\| 4f^N\alpha'[S'L']J'\right\rangle\right|^2 \qquad \textbf{Eq. 1-1}$$

where exemplary $[\Omega_2 \quad \Omega_4 \quad \Omega_6] = [6.07 \quad 3.05 \quad 10.52]$ Judd-Ofelt parameters for fluorides were considered (unless explicitly indicated for other matrix) and tensor $U_{2,4,6}$ values for given transitions were based on Ref. [4]. All transitions were confronted with the ones observed experimentally, and their intensities were qualitatively presented in the diagrams through the corresponding line thickness. The feasible cross-relaxation processes, which are critical for the energy looping and feeding the intermediate energy levels suitable for further ESA processes, were also indicated together with line strengths and energy mismatch. All these data have been additionally tabulated below the subsequent graphs for each of the analysed ions. The theoretical values of A_{ij} gives rough estimation on the line strength and the probability of given transition, which should allow to predict and design PA processes in new materials.

1.1 Praseodymium ions – Pr^{3+}

Praseodymium trivalent ion (Pr^{3+}) is broadly utilized in spectroscopy [5–8] (performed even on the single ion level [9]), optoelectronics [10,11] and laser techniques [12–15], including systems with surface plasmon resonance enhanced performance [16]. Moreover, as these ions can be efficiently excited in NIR region corresponding to the transmission window of biological tissues [17], utilization of Pr^{3+} doped nanocrystalline matrices was proposed in bio detection and bioimaging [18,19]. Materials doped with Pr^{3+} ions were also tested as the promising candidates for applications in therapeutics, especially as the sensitizers in radiotherapy [20,21]. Praseodymium trivalent ion (Pr^{3+}) is broadly utilized in spectroscopy [5–8] (performed even on the single ion level [9]), optoelectronics [10,11] and laser techniques [12–15], including systems with surface plasmon resonance enhanced performance [16]. Moreover, as these ions can be efficiently excited in NIR region corresponding to the transmission window of biological tissues [17], utilization of Pr^{3+} doped nanocrystalline matrices was proposed in bio detection and bioimaging [18,19]. Materials doped with Pr^{3+} ions were also tested as the promising candidates for applications in therapeutics, especially as the sensitizers in radiotherapy [20,21].

Particular interest in spectroscopic research of Pr^{3+} doped materials was motivated by the fact that blue, green and red emission can be obtained via visible and NIR excitations.[14,22] , as shown in the **Figure S1**. One of the most common ways to excite Pr^{3+} ions is to directly pump from the $^3H_4$ ground state to the higher: $^3P_{0,1,2}$ levels (using 440 – 480 nm light or via upconversion mechanism using combination of 1010 nm and 835 nm light beams with $^1G_4$ level as the intermediate state) or $^1D_2$ level (using ~590 nm light) [5,6,14,23,24]. The resulting emission occurs mainly from $^3P_0$ state transitions to $^3H_{4,5,6}$ or $^3F_{0,1,2}$ levels, emitting in blue (~480 nm, the most intense typically), green (~540 nm) and orange (~610 nm) spectral ranges for end states $^3H_4$, $^3H_5$, $^3H_6$, respectively, as well as producing red light (~640 nm, ~695 nm and ~720 nm) for $^3F_2$, $^3F_3$ and $^3F_4$ terminating levels, respectively [5,14]. Alternatively, orange (~600 nm), red (~700 nm) or NIR (~810 nm and ~870 nm) emissions corresponding to transitions from $^1D_2$ level to $^3H_4$, $^3H_5$, $^3H_6$ and $^3F_2$ states, respectively [5]. However, it is worth to note that also IR emissions, promising for applications as the laser sources, can be obtained from Pr^{3+} ions, namely from transitions occurring between lower laying energy levels: $^1G_4$, $^3F_{0,1,2}$ and $^3H_{4,5,6}$, giving numerous emission bands, with the most important: 1.35 µm, 1.6 µm, 1.7 – 2.6 µm and 3 – 5 µm [25,26]. Other efficient way of pumping Pr^{3+} is ETU, typically with Yb^{3+} ions employed as sensitizers. In such systems $^2F_{5/2}$ state in Yb^{3+} can be populated by 940-980 nm laser light, and then their energy can be transferred non radiatively to nearby Pr^{3+} ion, increasing occupation of $^1G_4$ state thereof [27]. Ions in this state (whose lifetimes are typically in the range of tens or hundreds of µs [28], which is long enough to perform such processes) can be then subsequently promoted to one of $^3P_{0,1,2}$ levels. Finally, it is worth to note that output from Pr^{3+} doped hosts, multicolour originally, can be further successfully tuned with dispersive and spectrally selective optical components to produce laser lines in desired spectral range [15]. Co-doping Pr^{3+} with Yb^{3+} ions can be also exploited in PA excitation scheme, when the excitation wavelength matches excited-state absorption in Pr^{3+} ions (e.g. ca.850nm) and does not fall into excitation bands of Yb^{3+} [29,30]. In such sensitized Photon Avalanche case described in **Chapter 6.3**, Yb^{3+} ions take over and accumulate part of Pr^{3+} energy in the long living $^2F_{5/2}$ state within, usually a few- to few-tens-fold larger number of Yb^{3+} ions (e.g. 20% Yb^{3+} vs 0.1 – 0.5% for Pr^{3+}), and then donate energy back to Pr^{3+} ions, and thus enhance energy looping. Similar sensitization should be feasible with other dopants such as Ho^{3+}, Tm^{3+} or Er^{3+}. Similar mechanism was demonstrated for $NaYF_4$ nanocrystals co-doped with Pr^{3+} and Yb^{3+} ions, where Yb^{3+} ions make migration network to propagate energy[31]. Due to the fact, this process is called as a Migrating Photon Avalanche (MPA). Initially, under excitation with 852 nm, few of ions in ground state absorption are excited to their excited state, namely Pr^{3+} to $^1G_4$ and Yb^{3+} to $^2F_{5/2}$. When Pr^{3+} ions are in $^3P_1$ higher-energy excited state (after ESA_1), the Yb^{3+} ions due to strong interaction with Pr^{3+} ions, can be promoted to the higher level, namely $^2F_{5/2}$ and in this time Pr^{3+} come back to $^1G_4$ level (CR_{10}). Subsequently, Yb^{3+} ions give energy to Pr^{3+} ions, populating $^1G_4$ excited state (CR_{12}). Increasing of number if ions in $^1G_4$ excited level leads to effective ESA transition, and then to observe PA emission from $^3P_0$, $^3P_1$ and $^1D_2$ levels. There was observed also PA emission from Yb^{3+} ions at 977 nm with slope reached 26.

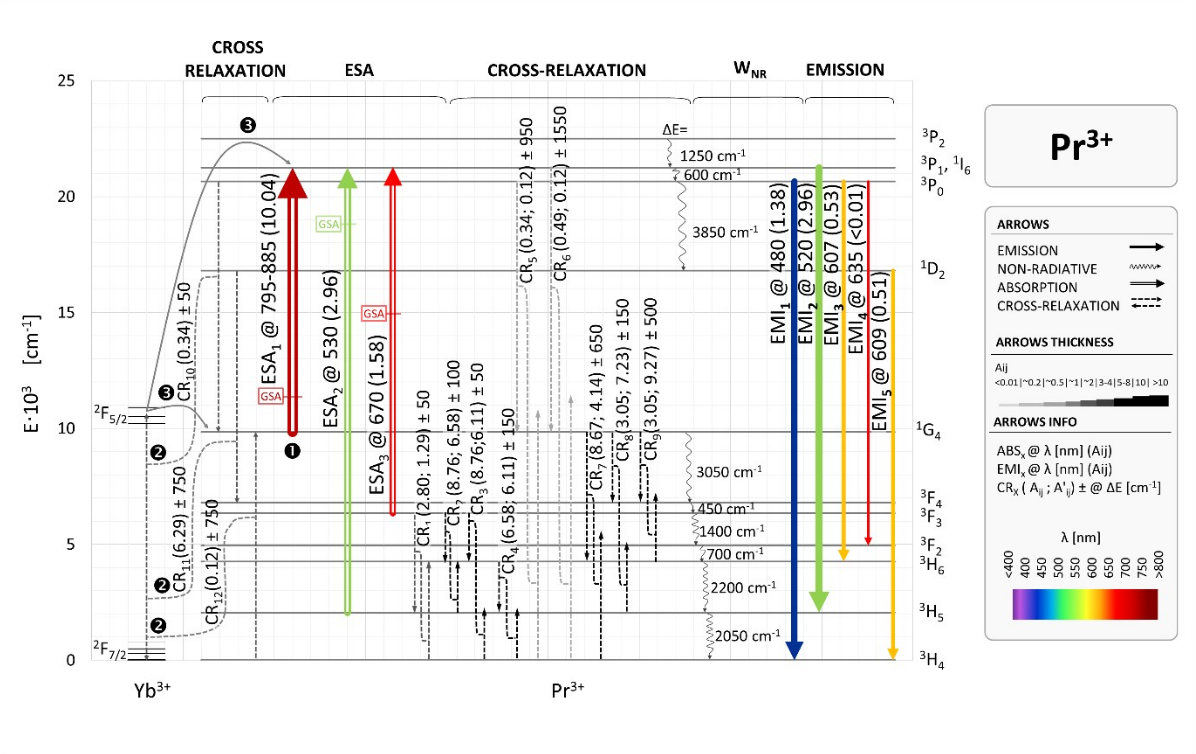

***Figure S1: Transitions and energy transfers suitable for PA** to occur in Pr^{3+} singly doped and Yb^{3+} and Pr^{3+} co-doped materials.*

One of the most promising advantages of Pr^{3+} ions is their broad ability to host processes necessary for nonlinear enhanced emission via photon avalanche mechanism. The very first report describing observation of the PA in lanthanides ions, published by Chivian *et al.* in 1979 [32], have concerned Pr^{3+} ions doped into $LaCl_3$ and $LaBr_3$ matrices (Pr^{3+} concentration of 4.88%). There were observed characteristic, highly nonlinear changes in optical properties of Pr-doped bulk crystals as a function of the power density of laser irradiation used for excite Pr^{3+} ions from $^3H_5$ to $^3P_1$ (ESA_2). Namely, when some threshold value of the excitation power density (in the range of 1.2 – 12.2 W/cm^2 in reported experiments) was exceeded, resulting intensity of green output of such system was rising avalanche-like and any minute variations of the laser irradiation power led to large changes of emitted light intensity. This phenomenon was caused by energy looping between three lowest energetic levels of Pr^{3+}, fed by efficient energy cross-relaxation between nearby ions, one in $^3H_6$ state, while the other in $^3H_4$ ground level (CR_4). As a result of this process, two ions in the intermediate $^3H_5$ level were obtained, promoting suitable conditions for absorption of laser irradiation and pumping into emitting states. Therefore, population of this level was doubled in each of iteration of such loop, playing a role of positive feedback and gain. This phenomenon occurring in $LaCl_3:Pr^{3+}$ and $BrCl_3:Pr^{3+}$ was studied in details in other works, where PA was also established by cross relaxation processes between $^3H_4$ and $^3H_6$ states, resulting in gained populating of $^3H_5$ levels [33,34], however also other similar CR mechanisms between lower energy levels could be involved in such operation (CR_{1-3}). [33,34], however also other similar CR mechanisms between lower energy levels could be involved in such operation (CR_{1-3}). Moreover, other mechanisms were investigated, like pumping the $^3F_3 \longrightarrow {}^3P_1$ transition (677 nm, ESA_3), resulting in the emission from $^3P_0 \longrightarrow {}^3F_2$ transitions (644 nm, EMI_4), with suggested PA processes multiplying population of the Pr^{3+} ions in $^3F_3$ state (for example CR_{5-7} processes, accompanied with MPR) [35]. It is worth to mention that the best performance of such system (25% conversion efficiency) has been found for the temperature of 80 K and it was gradually decreasing with rising temperature till 210 K, where emission was terminated [35]. It is worth to mention that the best performance of such system (25% conversion efficiency) has been found for the temperature of 80 K and it was gradually decreasing with rising temperature till 210 K, where emission was terminated [35].

Observations of PA were successfully carried out also in others Pr^{3+}-doped hosts, such as fibers, SiO$_2$ glass fibers [36], where critical threshold pumping power was estimated to be lower than 0.5 W/cm^2. Numerous experiments were conducted also for systems, where Pr^{3+} and Yb^{3+} ions were co-doped in such hosts like LiYF$_4$ [37], ZBLAN (ZrF4, BaF$_2$, LaF$_3$, AlF$_3$, NaF) fibers [13], Y$_2$O$_3$ [38] or BaY$_2$F$_8$ [22,39]. Co-doping with Yb^{3+} ions, due to good matching of its $^2F_{7/2} \longrightarrow {}^2F_{5/2}$ transition energy with, both, $^3H_4 \longrightarrow {}^1G_4$ (GSA$_1$) and $^1G_4 \longrightarrow {}^3P_0$ (ESA$_1$) transitions energies, supported with rather long lifetime of the $^1G_4$ (in the range of tens of µs typically, dependent on crystal matrix being used [28]), enables utilization of this level as the reservoir state for photon avalanche, populated by the cross relaxation between ground $^3H_4$ state and one of the $^3P_{0,1,2}$ levels (CR$_{5\text{-}7}$). Furthermore, it was possible to obtain PA in such systems with much lower concentrations of Pr^{3+} ions than in systems doped with Pr^{3+} only. Moreover, in the selected cases, Pr^{3+} doped PA-hosting systems were utilized as the laser sources [13,22,33,35]. Despite numerous possible scenarios of such Pr^{3+}-doped systems pumping, in most of the cases the resulting emitting state was the metastable $^3P_0$ level, and several emission peaks in visible range, including blue, green, orange and red was observed.

Table S1: Collection of transitions suitable for obtaining photon avalanche in Pr^{3+} doped materials. *λ/ ν denote excitation/emission wavelength in nm/cm^{-1}; $\Delta\nu$ denotes either energy mismatch (for CR) or energy gap (for GSA, ESA, EMI) between respective levels; Data for LiYF$_4$ matrix : Ω_2=0 Ω_4=8.07 Ω_6=7.32[40]. A_{ij} defined by Eq.1.1.* [40]

	Term	Term	λ	ν	A_{ij}	Comment, Ref
	Start	End	[nm]	[cm^{-1}]		
Excitation						
ESA$_1$	$^1G_4$	$^3P_1$	795-885	11400	10.04	
ESA$_2$	$^3H_5$	$^3P_1$	530	19200	2.96	[32,33,38]
ESA$_3$	$^3F_3$	$^3P_1$	670	14900	1.58	[35,36]
Looping				$\Delta\nu$		
CR$_1$	($^3F_3$; $^3H_4$)	($^3H_5$; $^3H_6$)		50	2.80; 1.29	[38]
CR$_2$	($^3F_3$; $^3H_5$)	($^3H_6$; $^3H_6$)		100	8.76; 6.58	
CR$_3$	($^3F_3$; $^3H_4$)	($^3H_6$; $^3H_5$)		50	8.76; 6.11	[38]
CR$_4$	($^3H_6$; $^3H_4$)	($^3H_5$; $^3H_5$)		150	6.58; 6.11	[32–34,38]
CR$_5$	($^3P_0$; $^3H_4$)	($^1G_4$; $^1G_4$)		950	0.34; 0.12	[37]
CR$_6$	($^3P_1$; $^3H_4$)	($^1G_4$; $^1G_4$)		1550	0.49; 0.12	[13,37]
CR$_7$	($^1G_4$; $^3H_4$)	($^3H_6$; $^3F_2$)		650	8.67; 4.14	[37]
CR$_8$	($^1G_4$; $^3H_5$)	($^3F_4$; $^3F_2$)		150	3.05; 7.23	
CR$_9$	($^1G_4$; $^3H_5$)	($^3F_4$; $^3F_4$)		1700		
CR$_{10}$	($^2F_{7/2}$; $^3P_0$)	($^2F_{5/2}$; $^1G_4$)		50	0.34	[31]
CR$_{11}$	($^2F_{7/2}$; $^1D_2$)	($^2F_{5/2}$; $^3F_4$)		750	6.29	[31]
CR$_{12}$	($^2F_{5/2}$; $^3H_4$)	($^2F_{7/2}$; $^1G_4$)		352	0.12	[31]
Emission			λ	ν		
EMI$_1$	$^3P_0$	$^3H_4$	480	20650	1.38	[15,31,36,38]
EMI$_2$	$^3P_1$	$^3H_5$	520	19200	2.96	[15,31]
EMI$_3$	$^3P_0$	$^3H_6$	607	15700	0.53	[15,22,32,39]
EMI$_4$	$^3P_0$	$^3F_2$	635	15700	<0.01	[13,15,22,34,35]
EMI$_5$	$^1D_2$	$^3H_4$	609	16420	0.51	[31]

1.2 Neodymium ions – Nd^{3+}

Nd^{3+} ions, most commonly excited via up-conversion mechanism under 808 nm, exhibit emission lines in visible, near infrared and infrared spectral regions [41,42]. Moreover, also upconversion emission (laser operation) in $LaF_3:Nd^{3+}$ at 380 nm (EMI_1- **Figure S2**. **Table S**2) was obtained after excitation with two photons in range of NIR and yellow region resonant with GSA $^4I_{9/2} \rightarrow {}^4F_{5/2}$ and with transition from $^4F_{3/2}$ to $^4D_{3/2}$ (ESA_4) respectively.[43]Nd^{3+} ions, most commonly ex[31]cited via up-conversion mechanism at λ=808 nm, exhibit emission lines in visible, near infrared and infrared spectral regions [41,42]. Moreover, also upconversion emission (laser operation) in $LaF_3:Nd^{3+}$ at 380 nm (EMI_1) was obtained after excitation with two photons in range of NIR and yellow region resonant with GSA $^4I_{9/2} \rightarrow {}^4F_{5/2}$ and with transition from $^4F_{3/2}$ to $^4D_{3/2}$ (ESA_4) respectively.[43]

In the case of neodymium, avalanche phenomenon was first observed in Nd-doped $LiYF_4$ bulk crystal pumped at 603.6 nm ($^4F_{3/2} \rightarrow {}^4D_{3/2}$ transition, ESA_4), leading to the anti-Stokes emission at 413 nm, corresponding to the $^2P_{3/2} \rightarrow {}^4I_{11/2}$ transition (EMI_2), where energy looping possibly occurs through the CR_2 mechanism resulting in (after MPR from close higher levels) increased $^4F_{3/2}$ metastable state population.[43] Similar mechanism was observed also in Nd-doped $LiKYF_5$ single crystal.[44] It is worth to mention that non-linear increase of emission intensity under increasing pump power were observed under NIR excitation at room temperature in the case of $LiLa_{1-x}Nd_xP_4O_{12}$ nanocrystalline powders, where emission was observed at 585, 656, 685 and 750 nm, corresponding to the $^2G_{7/2} + {}^4G_{5/2} \rightarrow {}^4I_{9/2}$, $^2G_{7/2} + {}^4G_{5/2} \rightarrow {}^4I_{11/2}$, $^4F_{9/2} \rightarrow {}^4I_{9/2}$ and $^4F_{7/2} + {}^2S_{3/2} \rightarrow {}^4I_{9/2}$ transitions, respectively. [41] However, the utilized excitation wavelength at 808 nm in this case was resonant with strong GSA transition in Nd^{3+}, which put in question the PA origin of the observed emission. Similarly, it was also known to use neodymium doping $NdAlO_3$ nanocrystalline powders, , which in high temperature of 350 °C and under (ground state matching) laser excitation at 808 nm corresponding to GSA exhibit bright yellow anti-Stokes emission, with intensity further increased by two orders of magnitude under vacuum conditions.[45] Furthermore, it is also possible to observe photon avalanche-like emission at room temperature in YAG co-doped with neodymium and ytterbium ions.[46] Some signs of PA behaviour were noticed (such as slow and pump power dependent rise times, relatively high pump power gains), but it is most probably not a clear photon avalanche. Moreover, in this configuration Yb^{3+} ions, absorbing 976 nm light, work as the sensitizers and Nd^{3+} plays the role of activator, giving unconventional emissions at 813 (EMI_{10}), 757 (EMI_9), 690 (EMI_8) and 597 nm (EMI_7) ($^4F_{5/2} + {}^2H_{9/2} \rightarrow {}^4I_{9/2}$, $^4F_{7/2} + {}^4S_{3/2} \rightarrow {}^4I_{9/2}$, $^4F_{9/2} \rightarrow {}^4I_{9/2}$ and $^4G_{5/2} + {}^4G_{7/2} \rightarrow {}^4I_{9/2}$ transitions, respectively). What is interesting, under excitation at 976 nm (as compared to 808 nm) no emission from level $^4F_{3/2}$ was observed, which is most probably related with the fact phonon emission ($Nd \rightarrow Yb + \hbar\omega$) is more probable than phonon absorption ($Yb + \hbar\omega \rightarrow Nd$). Moreover, in the reported power dependence measurements nonlinear s-shape dependence was observed with the maximal slope of around 5. Interestingly, the nonlinearity of the process was rising proportionally to the rising emitting state energy. Photon avalanche like upconversion was also observed in neodymium aluminum borate $NdAl_3(BO_3)_4$ nanoparticles doped with Nd^{3+} ions under excitation at 1064 nm[47,48]. This mechanism relays on an initial sideband ground state absorption leading to the population of metastable $^4F_{3/2}$ level and excited state absorption $^4I_{11/2} \rightarrow {}^4F_{3/2}$ (ESA_3). After cross-relaxation (CR_1) looping the population of the $^4I_{15/2 \ldots 11/2}$ state can be doubled and every iteration contribute to the enhancement of luminescence intensity by photon-avalanche-like emission. Emission bands at 880 (EMI_{12}), 810 (EMI_{10}), 750 (EMI_9), 690 (EMI_8) as well as at 660 (EMI_6), 600 (EMI_5) and 536 nm (EMI_4) (**Figure S2**) were observed and it was noted, that non-radiative relaxations cause increase of temperature of researched samples and simultaneously luminescence intensity increase is reported.[48] Similarly, PA-like process under excitation with 1064 nm was investigated involving external heating and also an increase of luminescence intensity with temperature increase was observed.[47] Moreover, PA threshold moved to lower values of pump power density with increasing the temperature. We suppose, that also ESA_1 and ESA_2 are likely after energy transfer from Yb^{3+} ions, excited as an activator, to Nd^{3+} ions. We decided to show cross-relaxations CR_3-CR_5 because these transitions seem useful to populate $^4I_{9/2}$ level for ESA_3. It is worth to notice that Nd^{3+} ions have found also application in the luminescence thermometry,[49] moreover their emission in the first and second biological window as well as absorption band λ = 808 nm do not overlap water absorption, which makes them desirable in bio-applications.[50,51] Theoretical modelling of the PA phenomenon in Nd^{3+} pumped via ESA at 1064 nm, beside great potential for PASSI,[52] exhibits also, due to thermal dependences of the essential processes incorporated in the PA, very promising features for thermometric utilizations, especially in single-band-ratiometric (SBR) luminescence thermometry approach, where feasible monitoring of ratio of the single emission band under two excitations types, GSA at 808 nm corresponds to $^4I_{9/2} \rightarrow {}^4F_{5/2}$ and ESA at 1064 nm (ESA_3) for $^4I_{11/2} \rightarrow {}^4F_{3/2}$, characterized with contrary thermal dependences, can be used to measure the temperature, with potential sub-micron resolutions.[42,53–55]

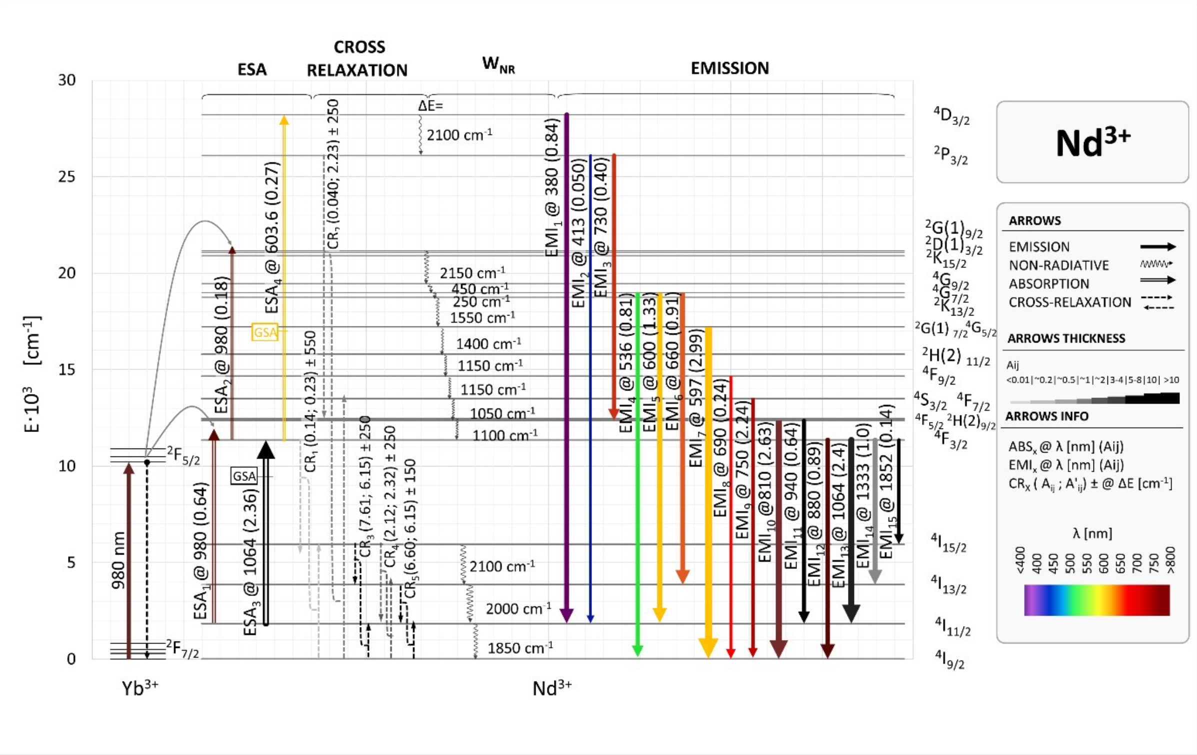

***Figure S2: Transitions and energy transfers suitable for PA** for Nd^{3+} doped materials.*

Table S2: Transitions suitable for obtaining photon avalanche in Nd^{3+} doped materials. *λ denotes excitation/emission wavelength in nm; $\Delta\nu$ denotes either energy mismatch (for CR) or energy gap (for GSA, ESA, EMI) between respective levels; Data for LiYF$_4$ matrix : Ω_2=1.9 Ω_4=2.7 Ω_6=5.0[40]. [40] A_{ij} defined by Eq.1.1.*

	Term	Term	λ	ν	A_{ij}	Comment, Ref
	Start	End	[nm]	[cm^{-1}]		
Excitation						
ESA$_1$	$^4I_{11/2}$	$^4F_{3/2}$	980	10204	0.64	
ESA$_2$	$^4F_{3/2}$	$^2G(1)_{9/2}$	980	10204	0.18	
ESA$_3$	$^4I_{11/2}$	$^4F_{3/2}$	1064	9398	2.36	52
ESA$_4$	$^4F_{3/2}$	$^4D_{3/2}$	603.6	16567	0.27	43,56
Looping				$\Delta\nu$		
CR$_1$	($^4F_{3/2;}$ $^4I_{9/2}$)	($^4I_{15/2}$; $^4I_{15/2}$)		550	0.14; 0.23	52
CR$_2$	($^2P_{3/2}$; $^4I_{9/2}$)	($^2H(2)_{9/2}$; $^4F_{7/2}$)		250	0.040; 2.23	43
CR$_3$	($^4I_{15/2}$; $^4I_{9/2}$)	($^4I_{13/2}$; $^4I_{11/2}$)		250	7.61; 6.15	
CR$_4$	($^4I_{15/2}$; $^4I_{9/2}$)	($^4I_{11/2}$; $^4I_{13/2}$)		250	2.12; 2.32	
CR $_5$	($^4I_{13/2}$; $^4I_{9/2}$)	($^4I_{11/2}$; $^4I_{11/2}$)		150	6.60; 6.15	
Emission				ν		
EMI$_1$	$^4D_{3/2}$	$^4I_{11/2}$	380	26316	0.84	43
EMI$_2$	$^2P_{3/2}$	$^4I_{11/2}$	413	24213	0.050	2,43,56
EMI$_3$	$^2P_{3/2}$	$^4F_{5/2}$	730	13699	0.40	57
EMI$_4$	$^4G_{7/2}$	$^4I_{9/2}$	536	19000	0.81	47,48
EMI$_5$	$^4G_{7/2}$	$^4I_{11/2}$	600	17150	1.33	47,48
EMI$_6$	$^4G_{7/2}$	$^4I_{13/2}$	660	15150	0.91	47,48
EMI$_7$	$^4G_{5/2}$	$^4I_{9/2}$	597	16750	2.99	47,48,58,59
EMI$_8$	$^4F_{9/2}$	$^4I_{9/2}$	690	14650	0.24	47,48,58,59
EMI$_9$	$^4F_{7/2}$	$^4I_{9/2}$	750	13500	2.24	47,48,58,59
EMI$_{10}$	$^4F_{5/2}$	$^4I_{9/2}$	810	12350	2.63	47,48,58,59
EMI$_{11}$	$^4F_{5/2}$	$^4I_{11/2}$	940	10638	0.64	60
EMI$_{12}$	$^4F_{3/2}$	$^4I_{9/2}$	880	11364	0.89	47,48,52
EMI$_{13}$	$^4F_{3/2}$	$^4I_{11/2}$	1064	9398	2.4	52
EMI$_{14}$	$^4F_{3/2}$	$^4I_{13/2}$	1333	7502	1.0	47,48,52
EMI$_{15}$	$^4F_{3/2}$	$^4I_{15/2}$	1852	5400	0.14	47,48,52

1.3 Samarium ions – Sm^{3+}

The luminescent properties of Sm^{3+} ions are relatively less frequently studied as compared to other lanthanide ions. The PA phenomenon was observed in Sm^{3+}-doped lanthanum bromide ($LaBr_3$) while investigating this material in the context of quantum counters development. This process was discovered at the temperature of 4.2 K, and under excitation at 593 nm (corresponding to the ESA $^6H_{7/2} \rightarrow {}^4G_{5/2}$ transition, **Figure S3**- ESA_3) emission line at 644 nm was reported (EMI_3) [61]. The avalanche origin of the emission was confirmed by both, rapid output intensity growth with rising excitation power density (with the threshold around 3 $kWcm^{-2}$) and significant slowing down of the emission risetime in the avalanching region. The proposed mechanism of PA contains, beside ESA pumping, also radiative and nonradiative energy dissipation to the low lying $^6H_{9/2}$ level, which then is able to initialize CR_8 with nearby ions in the ground state, leading to multiplying $^6H_{7/2}$ level population and therefore providing environment for the PA-powering energy looping.

It is worth to notice that beside of the mentioned PA mechanism, set of other hypothetical pumping and looping schemes might be proposed in Sm^{3+}. Rich structure of energy levels of these ions can host numerous possible CR processes with very low energy mismatch. Especially, there are accessible CR including the emitting metastable $^4G_{5/2}$ state(CR_{1-7}), providing suitable way to utilize part of its energy to spread the population of the ions in the lower laying energy levels (which also can exchange energy to populate given state considered as the starting one for ESA pumping). However, rich energetic structure is on the other hand one of the most important limitations for PA performance in Sm^{3+}, as the ESA transitions are in most of the cases also close to the resonance with GSA transitions present in the system, as shown for $ESA_{1,2}$ transitions.

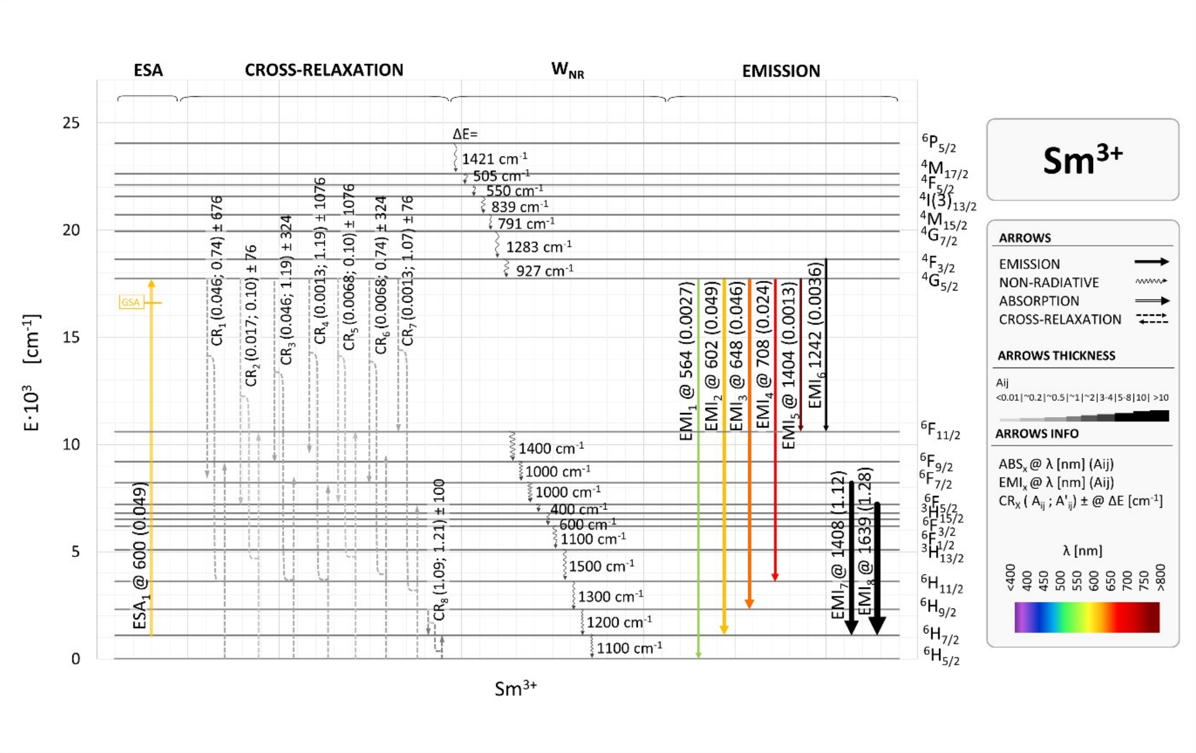

*Figure S3: **Transitions and energy transfers suitable for PA** for Sm^{3+} doped materials.*

Table S3: Transitions and energy transfers suitable for Sm^{3+} doped materials. λ/ ν denote excitation/emission wavelength in nm/cm^{-1}; $\Delta\nu$ denotes either energy mismatch (for CR) or energy gap (for GSA, ESA, EMI) between respective levels; Data for glasses phosphate matrix $\Omega_2 = 1.50$; $\Omega_4=3.75$; $\Omega_6= 1.89$. A_{ij} defined by Eq.1.1.

	Term	Term	λ	ν	A_{ij}	Comment
	Start	End	[nm]	[cm^{-1}]		
Excitation						
ESA_1	$^6H_{7/2}$	$^4G_{5/2}$	600	16620	0.049	
Looping				$\Delta\nu$		
CR_1	($^4G_{5/2}$;$^6H_{5/2}$)	($^6F_{7/2}$;$^6F_{9/2}$)		676	0.046;0.74	[62,63]
CR_2	($^4G_{5/2}$;$^6H_{5/2}$)	($^6F_{5/2}$;$^6F_{11/2}$)		76	0.017;0.10	[64,65] [64,65]
CR_3	($^4G_{5/2}$;$^6H_{5/2}$)	($^6F_{9/2}$;$^6F_{7/2}$)		324	0.046;1.19	[64,65]
CR_4	($^4G_{5/2}$;$^6H_{5/2}$)	($^6F_{11/2}$;$^6F_{7/2}$)		1076	0.0013;1.19	[64]
CR_5	($^4G_{5/2}$;$^6H_{5/2}$)	($^6F_{5/2}$;$^6F_{11/2}$)		1076	0.0068;0.10	[62]
CR_6	($^4G_{5/2}$;$^6H_{5/2}$)	($^6F_{7/2}$;$^6F_{9/2}$)		324	0.0068;0.74	[65]
CR_7	($^4G_{5/2}$;$^6H_{5/2}$)	($^6F_{11/2}$;$^6F_{5/2}$)		76	0.0013;1.07	[65]
CR_8	($^6H_{9/2}$;$^6H_{5/2}$)	($^6H_{7/2}$; $^6H_{7/2}$)		100	1.09;1.21	
Emission				ν		
EMI_1	$^4G_{5/2}$	$^6H_{5/2}$	564	17720	0.0027	[62,63,65]
EMI_2	$^4G_{5/2}$	$^6H_{7/2}$	602	16620	0.049	[62,63,65]
EMI_3	$^4G_{5/2}$	$^6H_{9/2}$	648	15420	0.046	[62,63,65]
EMI_4	$^4G_{5/2}$	$^6H_{11/2}$	708	14120	0.024	[62,63]
EMI_5	$^4G_{5/2}$	$^6F_{11/2}$	1404	7120	0.0013	[62]
EMI_6	$^4F_{3/2}$	$^6F_{11/2}$	1242	8050	0.0036	[62]
EMI_7	$^6F_{7/2}$	$^6H_{7/2}$	1408	7100	1.12	[62]
EMI_8	$^6F_{5/2}$	$^6H_{7/2}$	1639	6100	1.28	[62]

1.4 Europium ions – Eu^{3+}

Moreover, beside the presence of a few possible ESA transitions in Eu^{3+}, a few promising schemes of CR that potentially may lead to multicolour photon avalanching in these ions (**Figure S4**). In particular, there can be found several CR (**Figure S4**- $CR_{1\text{-}8}$) leading to increased populations of the lower excited states (^7F_J, J = 3,…,6) using the matching energy portions from transitions between the $^5D_{J'}$ (J'=0,…,3) higher levels, as well as set of internal CRs between the ^7F_J levels ($^7F_3$; $^7F_0$) → ($^7F_2$; $^7F_2$) or ($^7F_5$; $^7F_0$) → ($^7F_3$; $^7F_3$). Their combination might provide suitable energy pathways to host the PA mechanism and thus offer broad palette of the visible emission achievable by avalanche pumping. Another profit of the mentioned possible pumping schemes originates from the fact that energy looping, as well as its spatial spreading and cumulation in the material, might not be competitive in respect to the emission, but might occur simultaneously, fuelling the CR not directly by the energy of the emitting state, but by the excess energy of the levels higher than the $^5D_0$ state. Therefore, double positive effect can be obtained – increasing population of the excited metastable state by promoting transfers from the ground state, and rising population of the emitting state, both at the same time, what could potentially result in brighter output than in typical PA materials.

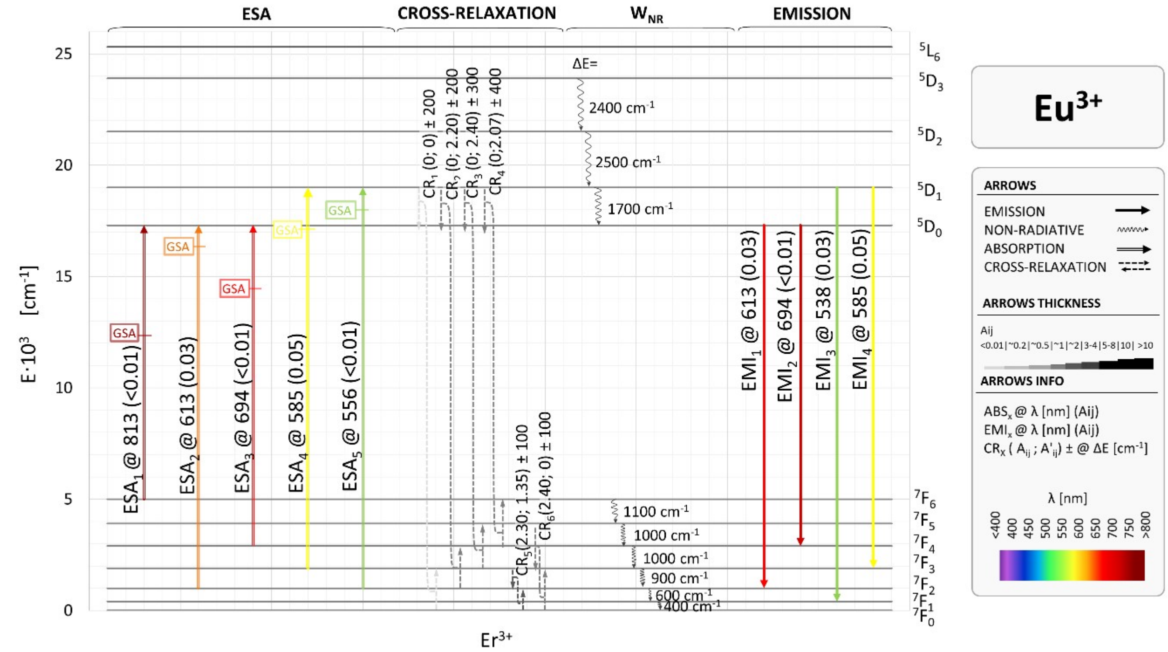

Figure S4: Transitions and energy transfers suitable for Eu^{3+} doped materials.

Table S4: Transitions and energy transfers suitable for Eu^{3+} doped materials. λ/ ν denote excitation/emission wavelength in nm/cm^{-1}; $\Delta\nu$ denotes either energy mismatch (for CR) or energy gap (for GSA,ESA,EMI) between respective levels; Data for Y_2O_3 matrix $\Omega_2 = 9.86$; $\Omega_4 = 2.23$; $\Omega_6 = 0.32$. A_{ij} defined by Eq.1.1.

	Term	Term	λ	ν	A_{ij}
	Start	End	[nm]	[cm^{-1}]	
Excitation					
ESA$_1$	$^7F_6$	$^5D_0$	813	12300	<0.01
ESA$_2$	$^7F_2$	$^5D_0$	613	16300	0.03
ESA$_3$	$^7F_4$	$^5D_0$	694	100	<0.01
ESA$_4$	$^7F_3$	$^5D_1$	585	17100	0.05
ESA$_5$	$^7F_2$	$^5D_1$	556	18000	<0.01
Looping				$\Delta\nu$	
CR$_1$	($^5D_1$;$^7F_0$)	($^5D_0$;$^7F_3$)		200	0;0
CR$_2$	($^5D_1$;$^7F_2$)	($^5D_0$;$^7F_4$)		200	0;2.20
CR$_3$	($^5D_1$;$^7F_3$)	($^5D_0$;$^7F_5$)		300	0;2.40
CR$_4$	($^5D_1$;$^7F_4$)	($^5D_0$;$^7F_6$)		400	0;2.07
CR$_5$	($^7F_3$; $^7F_0$)	($^7F_2$; $^7F_2$)		100	2.30;1.35
CR$_6$	($^7F_5$; $^7F_0$)	($^7F_3$; $^7F_3$)		100	2.40;0
Emission				ν	
EMI$_1$	$^5D_0$	$^7F_2$	613	16300	0.03
EMI$_2$	$^5D_0$	$^7F_4$	694	14400	<0.01
EMI$_3$	$^5D_1$	$^7F_1$	538	18600	0.03
EMI$_4$	$^5D_1$	$^7F_3$	585	17100	0.05

1.5 Terbium ions – Tb^{3+}

Based on the Tb^{3+} energy levels diagram and on the possibility of ESA-type pumping of the emitting states, one can propose promising pathway to provide avalanching in matrices doped with these ions. In the probable scenario the pumping from $^7F_5$ or $^7F_4$ (ESA_1 and ESA_3, respectively) leads to pumping the $^5D_3$ state, which is then followed by emission or, alternatively, by the CR_7 process. CR_7 in turn results in increased population of the $^7F_0$ level, which is relaxing fast to the both ESA-starting states via MPR supported also by set of possible CR ($CR_{1\text{-}6}$) providing further promotion of the nearby ions from ground state to the higher ^7F_J (J=1..6) levels. Nevertheless, photon avalanching process has not been observed in materials doped with terbium ions. However, similarly to the GSA from $^7F_6$ level, also ESA transitions from $^7F_5$ are observed in terbium ions, both of them populating the two main emitting $^5D_3$ and $^5D_4$ levels in terbium ions. Decay time of $^5D_4$ level is about one order of magnitude longer than in the case of $^5D_3$ level in wide range of temperatures.[66] It motivated the studies on utilization of Tb^{3+}-doped materials in the luminescence thermometry, especially in the approach so-called single-band-ratiometric thermometry, where temperature can be estimated from the intensity ratio of the chosen single emission band under two different excitation wavelengths, corresponding to GSA and ESA pumping schemes, typically, as it has been shown by J. Drabik et al. for $KLaP_4O_{12}$ doped with Tb^{3+} ions.[67] They observed emission associated with $^5D_4 \rightarrow {}^7F_3$ transition originating from GSA-type excitation with λ_{GSA} = 485 nm ($^7F_6 \rightarrow {}^5D_4$ transition), as well as from ESA-type pumping with λ_{ESA} = 543 nm ($^7F_5 \rightarrow {}^5D_4$ transition) [67]. The enhancement of the emission intensity after ESA excitation with increasing temperature was observed due to increased probability of thermal promotion of the electrons from ground level ($^7F_6$) to the first excited level ($^7F_5$), according to the Boltzmann distribution. Simultaneously, due to the same reason, the GSA-pumped emission intensity exhibits opposite behaviour, as population of the initial state for this process is reduced with the rising temperature. These are transitions from $^5D_4$ level to $^7F_3$, $^7F_2$, $^7F_1$, $^7F_0$ at 620, 650, 670 and 680 nm, respectively, from which $^5D_4 \rightarrow {}^7F_3$ is the most intense. Besides the mentioned transitions, the most effective emission in terbium ions is the $^5D_4 \rightarrow {}^7F_5$ transition at 540 nm. Similar SBR approach was applied for other wavelengths corresponding to GSA ($^7F_6 \rightarrow {}^5D_3$) and ESA ($^7F_5 \rightarrow {}^5D_3$) transitions in nanothermometers, where good 3.2%/°C thermometric sensitivity was achieved.[66] Likewise, Tb^{3+} ions were applied also in other matrices, namely Y_2O_3 and Lu_2O_3, where luminescence of defects increased and simultaneously Tb^{3+} luminescence decreased with temperature. [68] For the designed thermometers 4.92%/°C and 2%/°C sensitivities were obtained respectively for Y_2O_3:0.05%Tb^{3+} and Lu_2O_3:0.5%Tb^{3+} nanocrystals. In $KTbP_4O_{12}$ co-doped with Cr^{3+} ions or with Eu^{3+} ions, sensitivities of 2.75%/°C and 1.36%/°C were achieved respectively. [69] [66] [67]

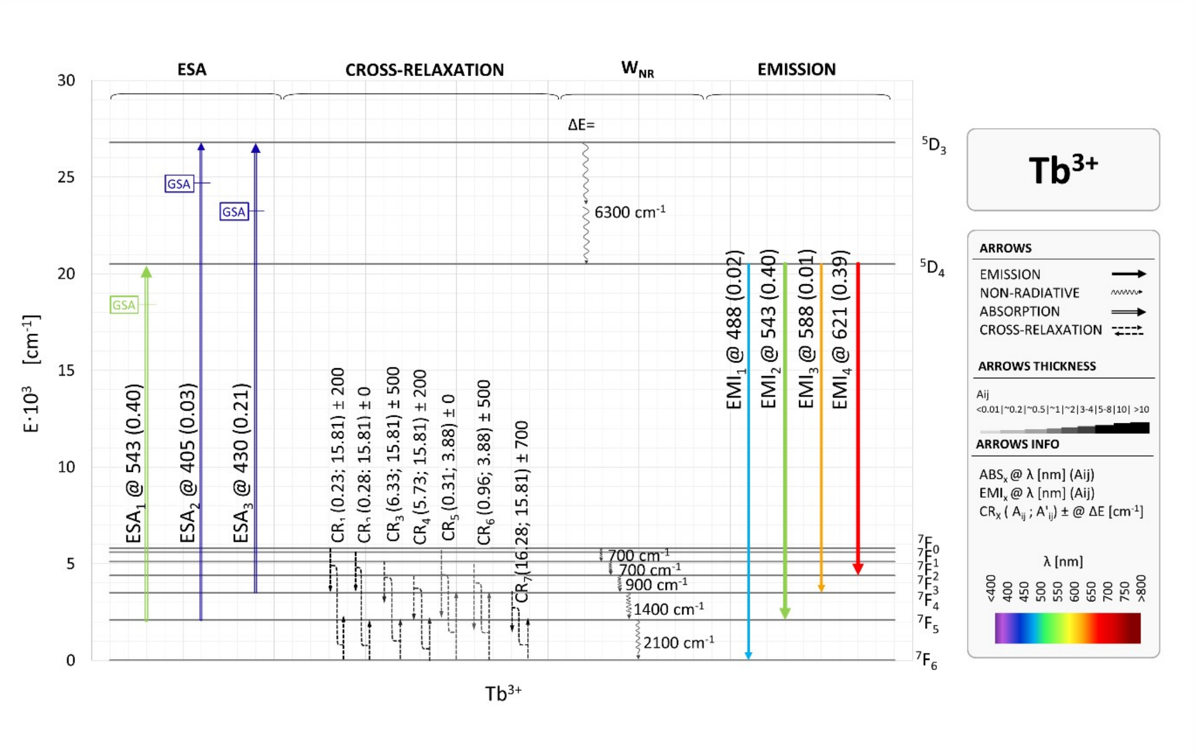

***Figure S5: Transitions and energy transfers suitable for PA** for Tb^{3+} doped materials.*

***Table S5: Transitions and energy transfers suitable for Tb^{3+} doped materials.** λ/ ν denote excitation/emission wavelength in nm/cm^{-1}; $\Delta\nu$ denotes either energy mismatch (for CR) or energy gap (for GSA, ESA, EMI) between respective levels; Data for matrix of $LiYF_4$: $\Omega_2 = 28.3$; $\Omega_4 = 1.65$; $\Omega_6 = 2.15$[40]. A_{ij} defined by **Eq. 1-1**.*

	Term Start	Term End	λ [nm]	ν [cm^{-1}]	A_{ij}
Excitation					
ESA_1	$^7F_5$	$^5D_4$	543	18400	0.40
ESA_2	$^7F_5$	$^5D_3$	405	24700	0.03
ESA_3	$^7F_4$	$^5D_3$	430	23300	0.21
Looping				$\Delta\nu$	
CR_1	($^7F_0$; $^7F_6$)	($^7F_4$; $^7F_5$)		200	0.23; 16
CR_2	($^7F_1$; $^7F_6$)	($^7F_4$; $^7F_5$)		0	0.28; 16
CR_3	($^7F_2$; $^7F_6$)	($^7F_4$; $^7F_5$)		500	6.30; 16
CR_4	($^7F_3$; $^7F_6$)	($^7F_5$; $^7F_5$)		200	5.70; 16
CR_5	($^7F_1$; $^7F_6$)	($^7F_5$; $^7F_4$)		0	0.31; 3.90
CR_6	($^7F_2$; $^7F_6$)	($^7F_5$; $^7F_4$)		500	0.96; 3.90
CR_7	($^5D_3$; $^7F_6$)	($^5D_4$; $^7F_0$)		500	1.50; 0.31
CR_8	($^5D_3$; $^7F_6$)	($^7F_0$; $^5D_4$)		500	0.02; 0.00
CR_9	($^7F_4$; $^7F_6$)	($^7F_5$; $^7F_5$)		700	16.28;15.81
Emission				ν	
EMI_1	$^5D_3$	$^7F_6$	373	26800	<0.01
EMI_2	$^5D_3$	$^7F_5$	405	24700	0.03
EMI_3	$^5D_3$	$^7F_4$	430	23300	0.21
EMI_4	$^5D_4$	$^7F_6$	488	20500	0.02
EMI_5	$^5D_4$	$^7F_5$	543	18400	0.40

EMI_6	$^5D_4$	$^7F_4$	588	17000	0.01
EMI_7	$^5D_4$	$^7F_3$	621	16100	0.39

1.6 Dysprosium ions – Dy^{3+}

There are no literature reports describing photon avalanche phenomenon in materials doped with dysprosium ions. However, analysing the energy diagram of Dy^{3+}, one may find a set of processes, which might lead to photon avalanching. First of all, structure of energetic levels in Dy^{3+}, with numerous lower levels and large energy gap separating them from the higher ones, opens the opportunity for hosting several ESA transitions (for example at 590 nm and 606 nm, marked as ESA_2 and ESA_3 in the **Figure S6**, respectively), which are simultaneously far from resonance with GSA, fulfilling one of the critical requirements to initialize PA. Moreover, some promising CR processes can be found, in which energy of $^4I_{15/2}$ and $^4F_{9/2}$ levels can be exchanged with neighbour ions in the ground state to promote the population of the intermediate level and enable ESA excitation.

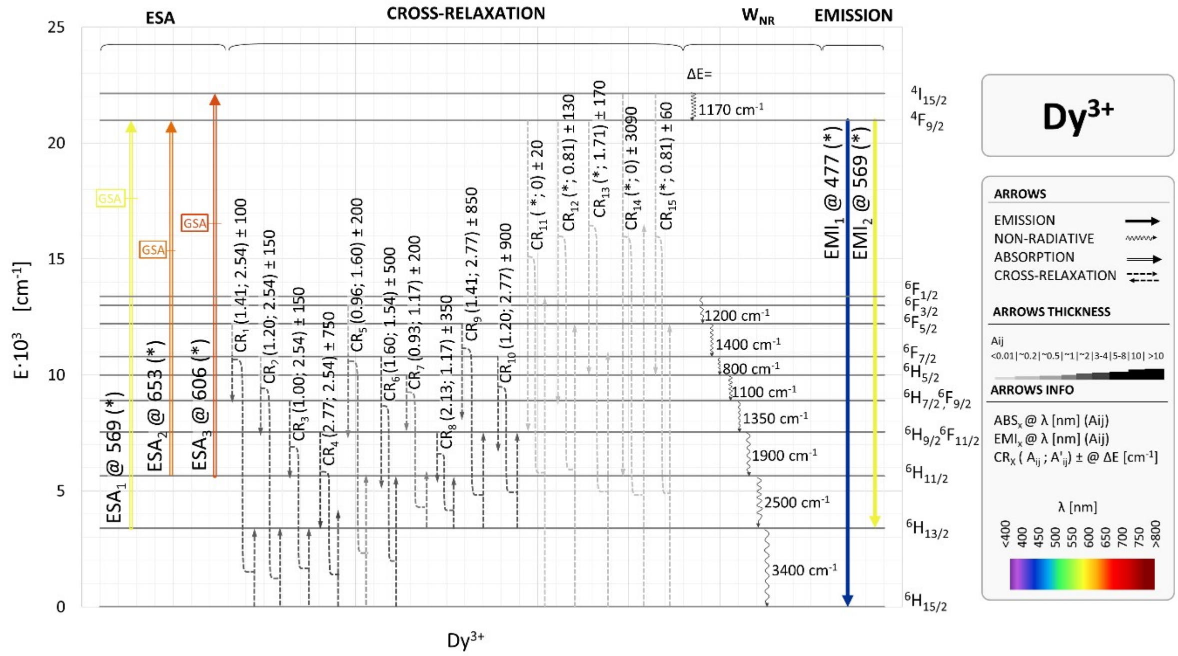

***Figure S6. Transitions and energy transfers suitable for Dy^{3+} doped materials.** Due to the lack of sufficient data, the oscillator strengths were not provided for Dy^{3+} ions. For the same reason, the line thicknesses do not qualitatively correspond to oscillator strengths*

Table S6. Transitions and energy transfers suitable for Dy^{3+} doped materials. λ/ ν denote excitation/emission wavelength in nm/cm^{-1}; $\Delta\nu$ denotes either energy mismatch (for CR) or energy gap (for GSA, ESA, EMI) between respective levels; Data for matrix of $LiYF_4$: $\Omega_2 = 2.01$; $\Omega_4 = 1.34$; $\Omega_6 = 2.39^{7070}.^{70}$. A_{ij} defined by Eq.1.1.

	Term	Term	λ	ν	A_{ij}
	Start	End	[nm]	[cm^{-1}]	

Excitation					
ESA$_1$	$^6H_{13/2}$	$^4F_{9/2}$	569	9600	No data
ESA$_2$	$^6H_{11/2}$	$^4F_{9/2}$	653	17570	No data
ESA$_3$	$^6H_{11/2}$	$^4I_{15/2}$	606	16490	No data
Looping				$\Delta\nu$	
CR$_1$	$(^6F_{5/2}; {}^6H_{15/2})$	$(^6H_{7/2}, {}^6F_{9/2}; {}^6H_{13/2})$		100	1.41, ; 2.54
CR$_2$	$(^6F_{7/2}; {}^6H_{15/2})$	$(^6H_{9/2}, {}^6F_{11/2}; {}^6H_{13/2})$		150	1.20; 2.54
CR$_3$	$(^6H_{7/2}, {}^6F_{9/2}; {}^6H_{15/2})$	$(^6H_{11/2}; {}^6H_{13/2})$		150	1.00, ; 2.54
CR$_4$	$(^6H_{9/2}, {}^6F_{11/2}; {}^6H_{15/2})$	$(^6H_{13/2}; {}^6H_{13/2})$		750	2.77 ; 2.54
CR$_5$	$(^6F_{3/2}; {}^6H_{15/2})$	$(^6H_{9/2}, {}^6F_{11/2}; {}^6H_{11/2})$		200	0.96; 1.60
CR$_6$	$(^6F_{7/2}; {}^6H_{15/2})$	$(^6H_{11/2}; {}^6H_{11/2})$		500	1.60; 1.54
CR$_7$	$(^6H_{5/2}; {}^6H_{13/2})$	$(^6H_{9/2}, {}^6F_{11/2}; {}^6H_{11/2})$		200	0.93; 1.17
CR$_8$	$(^6H_{9/2}, {}^6F_{11/2} ; {}^6H_{13/2})$	$(^6H_{11/2}; {}^6H_{11/2})$		350	2.13; 1.17
CR$_9$	$(^6F_{5/2};{}^6H_{13/2})$	$(^6H_{7/2}, {}^6F_{9/2}; {}^6H_{9/2}, {}^6F_{11/2})$		850	1.41; 2.77
CR$_{10}$	$(^6F_{7/2};{}^6H_{13/2})$	$(^6H_{9/2}, {}^6F_{11/2}; {}^6H_{9/2}, {}^6F_{11/2})$		900	(1.20; 2.77)
CR$_{11}$	$(^4F_{9/2};{}^6H_{15/2})$	$(^6H_{9/2}, {}^6F_{11/2}; {}^6F_{1/2})$		20	(-; 0)
CR$_{12}$	$(^4F_{9/2};{}^6H_{15/2})$	$(^6H_{7/2}, {}^6F_{9/2}; {}^6F_{5/2})$		130	(-; 0.81)
CR$_{13}$	$(^4F_{9/2};{}^6H_{15/2})$	$(^6H_{5/2}; {}^6F_{7/2})$		170	(-; 1.71)
CR$_{14}$	$(^4I_{15/2};{}^6H_{15/2})$	$(^6H_{11/2}; {}^6F_{1/2})$		3090	(-; 0)
CR$_{15}$	$(^4I_{15/2};{}^6H_{15/2})$	$(^6H_{5/2}; {}^6F_{5/2})$		60	(-; 0.81)
Emission				ν	
EMI$_1$	$^4F_{9/2}$	$^6H_{15/2}$	477	20747	No data
EMI$_2$	$^4F_{9/2}$	$^6H_{13/2}$	569	17575	No data

1.7 Holmium ions – Ho^{3+}

PA in holmium doped materials was first observed in 1999 in YAP crystal [71] and ZBLAN glass [72]. Holmium is well-known upconverting ion, which, sensitized by Yb, exhibits mostly green emission at 540 nm ($^5F_4$,$^5S_2 \rightarrow {}^5I_8$, EMI$_4$),[73] accompanied with red 650 nm emission ($^5F_5 \rightarrow {}^5I_8$, EMI$_3$) ref and NIR emission at 1185 nm ($^5I_6 \rightarrow {}^5I_8$, EMI$_1$)[73–75] . Introduced the doping of ytterbium opened up additional possibilities for cross relaxation in this system , which affects a much more intense, $^5S_2$ level emission Since mid- 1960s Ho^{3+} doped crystals were utilized in laser applications, commonly with garnet hosts: YAG, YSGG and YSAG [76–78] Although in the first Ho-based designs low temperatures were required, nowadays holmium lasers operate at room temperature and are the ones of the most widespread solid lasers with numerous applications in e.g. medical tretments[79].

Complex system of the energy levels in Ho^{3+}, with numerous homogeneously arranged and similarly separated levels, promotes presence of several possible CR transitions between them and suggests possibility of PA hosting for this ion. One of the earliest demonstrations of the avalanche-like energy looping or PA phenomenon in Ho^{3+} doped materials were reported in 1996 for ZBLAN host,[80] followed by the reports for the YAP[81] crystal and the ZBLAN glass[82] in 1999.[80] [8182] Similar mechanism was employed for these experiments, based on the ESA pumping from the first (and long-living) excited state ($^5I_7$, playing the role of the metastable state) to the $^5G_6$ + $^5F_1$ levels (~585 nm) followed by the fast non-radiative transitions to the $^5S_2$ state and green emission centred at 545 nm (although also red emission at 660 nm was observed). However, the used excitation line is also in resonance with $^5I_6 \rightarrow {}^5G_4 + {}^3K_7$ ESA transition, leading to populating the higher energy levels. Nevertheless, despite presence of clear pumping threshold combined with PA characteristic features in the emission rise time dynamics, it is not possible to define only one CR transition resulting in direct doubling the population of ions in metastable state and starting from the ground end the emitting levels. More probable is the situation which requires a combination of several elemental possible CR transitions giving finally the desired energy looping in the ($^5S_2$; $^5I_8$) → ($^5I_7$; $^5I_7$) scheme [71,83,84]. Interestingly, due to presence of matching transitions, the improved operation of such systems was demonstrated with co-doping with Tm^{3+} ions [71,83,84]. The early 2000s, next to adaptation of the previous pumping scenario to the new materials, like $LiYF_4$, YAG and YAP,[85] brought also other approaches to the PA investigations in Ho-doped materials. In $LiYF_4$ crystals Kück and Sokólska observed the photon avalanche emission at 545 nm (however also much weaker emissions at 650 nm and 485 nm were measured) under 750 nm photoexcitation [86]. The used pump line wavelength, well fitted to the ESA transition, was at the same time not far from the resonance with GSA (~740 nm), nonetheless detailed studies evidenced significant differences in the luminescence rising kinetics during varying the excitation line spectral position between the ESA and GSA resonant ones, suggesting avalanche pumping in the former case. Green emission after ESA-resonant excitation at 750 nm was also observed in the broad set of Ho-doped materials [86–89]. Interestingly, similar pumping scheme based on 750 nm ESA excitation was also utilized in the Ho-Yb co-doped system, in which Yb ion, with the energy gap matching to $^5S_2$+$^5F_4$ → $^5I_6$ and $^5I_8$ → $^5I_6$ transitions in Ho, was used as the mediator increasing the number possible avalanche-powering CR events[90,91] . The same dopant combination was applied also for observation of non-linear responses from Gd_2O_3 nanocrystals (~100 nm in size), however this time the 976 nm excitation was used, fitted into the Yb absorption and close to resonance in selected ESA transitions in Ho[92].

Because Ho^{3+} is one of the most efficient upconverting ions, the presence of Yb^{3+} sensitizer should have important contribution in PA excitation. The scheme of such sensitized PA emission was indicated on **Figure S7**. First, weak ESA excitation (e.g. 746 nm) initiates the looping which partially populates the $^5I_5$ level. Because no concentration quenching in Yb^{3+} occurs (energy gap between the two levels is much higher than the matrix phonons) and Yb^{3+} are known for its high absorption cross-section, the energy of $^5I_5$ Ho^{3+} level may be effectively transferred to quasi-resonant $^2F_{5/2}$ level in Yb^{3+} ions (3). This will be followed by efficient energy donation from excited Yb^{3+} ions back to neighbour Ho^{3+} ions (2) like in conventional ETU upconversion process. In consequence the intermediate $^5I_7$, $^5I_6$ levels of Ho^{3+} ions should be populated aiming to increase the absorption cross section for ESA_{1-4} . These preliminary steps, should eventually enhance energy looping between Ho^{3+}-Ho^{3+} pairs.[90,93]

Migrating photon avalanche was also observed for Ho^{3+} ions using energy transfer between Yb^{3+} ions after excitation with 852 nm. Ho^{3+} ions were placed in four-layer structure, between layers connecting Yb^{3+} and Pr^{3+} ions: $NaYF_4$:Yb/Pr(15/0.5%) @ $NaYF_4$:Yb/Ho(3/4%) @ $NaYF_4$:Yb/ Pr(15/0.5%) @ $NaLuF_4$. Thanks to effective PA process obtained in core, the energy was transferred to Ho^{3+} ions and then PA emission from Ho^{3+} at 541nm ($^5S_2$/$^5F_4$→$^5I_8$) and 646 nm ($^5F_5$→$^5I_8$) was observed with slopes reached 28. As a comparison there were prepared nanoparticles with single Ho^{3+} as well as co-doped with Ho^{3+} and Yb^{3+} ions and in both cases PA emission under 852nm excitation was not observed.

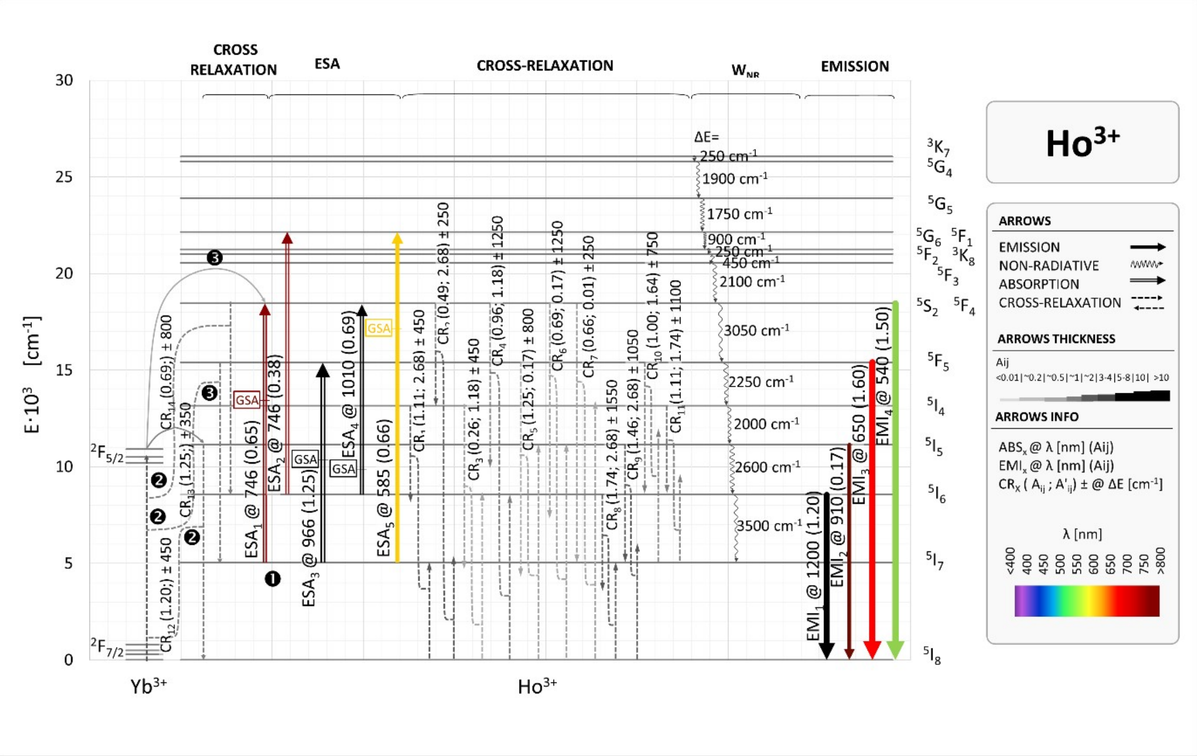

Figure S7. Transitions and energy transfers suitable for PA *to occur in Ho^{3+} singly and Yb^{3+}-Ho^{3+} co-doped doped materials.*

Table S7. Collection of transitions suitable for obtaining photon avalanche in Ho^{3+} doped materials. *λ/ν denote excitation/emission wavelength/energy in nm/cm^{-1}; $\Delta\nu$ denotes either energy mismatch (for CR) or energy gap (for GSA, ESA, EMI) between respective levels; Data for matrix of LiYF$_4$: $\Omega_2 = 1.16$; $\Omega_4 = 1.62$; $\Omega_6 = 1.60$[4]. A$_{ij}$ defined by Eq.1.1.*

	Term	Term	λ	ν	A$_{ij}$
	Start	End	[nm]	[cm^{-1}]	
Excitation					
ESA$_1$	$^5I_7$	$^5S_2$,$^5F_4$	746	13400	0.65
ESA$_2$	$^5I_6$	$^5G_6$,$^5F_1$	746	13600	0.38
ESA$_3$	$^5I_7$	$^5F_5$	966	10350	1.25
ESA$_4$	$^5I_6$	S_2 ,$^5F_4$	1010	9900	0.69
ESA$_5$	$^5I_7$	$^5G_6$	585	17094	0.66
Looping				$\Delta\nu$	
CR$_1$	($^5I_4$; $^5I_8$)	($^5I_6$; $^5I_7$)		450	1.11; 2.68
CR$_2$	($^5S_2$,$^5F_4$;$^5I_8$)	($^5I_4$; $^5I_7$)		250	0.49; 2.68
CR$_3$	($^5I_4$; $^5I_8$)	($^5I_7$; $^5I_6$)		450	0.26;1.18
CR$_4$	($^5S_2$,$^5F_4$; $^5I_8$)	($^5I_5$; $^5I_6$)		1250	0.96; 1.18
CR$_5$	($^5F_5$; $^5I_8$)	($^5I_7$; $^5I_5$)		800	1.25; 0.17
CR$_6$	($^5S_2$,$^5F_4$; $^5I_8$)	($^5I_6$; $^5I_5$)		1250	0.69;0.17
CR$_7$	($^5S_2$,$^5F_4$; $^5I_8$)	($^5I_7$; $^5I_4$)		250	0.66;0.01

CR$_8$	($^5I_6$; $^5I_8$)	($^5I_7$; $^5I_7$)		1550	1.74;2.68
CR$_9$	($^5I_5$; $^5I_8$)	($^5I_7$; $^5I_7$)		1050	1.46;2.68
CR$_{10}$	($^5F_5$; $^5I_8$)	($^5I_6$; $^5I_5$)		750	1.00;1.64
CR$_{11}$	($^5I_4$; $^5I_8$)	($^5I_6$; $^5I_6$)		1100	1.11;1.74
CR$_{12}$	($^2F_{5/2}$; $^5I_8$)	($^2F_{7/2}$; $^5I_5$)		450	1.20;
CR$_{13}$	($^2F_{5/2}$; $^5I_7$)	($^2F_{7/2}$; $^5F_5$)		350	1.25;
CR$_{14}$	($^2F_{5/2}$; $^5I_6$)	($^2F_{7/2}$; $^5S_2$,$^5F_4$)		800	0.69;
Emission				ν	
EMI$_1$	$^5I_6$	$^5I_8$	1200	8550	1.20
EMI$_2$	$^5I_5$	$^5I_8$	910	11150	0.17
EMI$_3$	$^5F_5$	$^5I_8$	650	15400	1.60 [31]
EMI$_4$	$^5S_2$,$^5F_4$	$^5I_8$	540	18450	1.50 [31]

1.8 Erbium ions – Er^{3+}

Erbium ions, characterized by strong green and red emissions, are one of the most broadly used ions in various aspects, including laser techniques, thermometry or photothermal therapy, especially in materials co-coped with Yb [94,95]. Their versatile utility motivated investigation of Er ions in the field of PA.

In LiYF$_4$ [96] and ZBLAN [97,98,99,100] glasses doped with erbium ions the PA phenomenon was observed for yellow and red excitations (at 579 nm [96–100] and 690 nm, ESA$_1$ and ESA$_3$, respectively), which correspond to the $^4I_{11/2} \rightarrow {}^2G_{9/2}$ ($^4G_{9/2}$ according to ref. 31) and $^4I_{11/2} \rightarrow {}^2H_{9/2}$ ($^2G(1)_{9/2}$ according to ref. 31) transitions, respectively. In LiYF$_4$ [96] and ZBLAN [97–100] glasses doped with erbium ions the PA phenomenon was observed for yellow and red excitations (at 579 nm [96–100] and 690 nm, ESA$_1$ and ESA$_3$, respectively), which correspond to the $^4I_{11/2} \rightarrow {}^2G_{9/2}$ and $^4I_{11/2} \rightarrow {}^2H_{9/2}$ transitions, respectively. As a result green emission at 550 nm ($^4S_{3/2} \rightarrow {}^4I_{15/2}$ transition, EMI$_4$ was observed). In contrast to other ions, the PA phenomenon in erbium doped materials is observed only above 130 K. This is due to the energy mismatch taking place in the CR process, which is compensated by photon absorption.

Because Er^{3+} is one of the most efficient upconverting ions, the presence of Yb^{3+} sensitizer should have important contribution in PA excitation scheme – the sequence of such sensitized PA emission was indicated on **Figure S8**. First, ESA$_2$ excitation (e.g. 690 nm) is weakly absorbed and initiates the looping (CR$_{3,4,5}$), which partially populates the $^4I_{11/2}$ level. Because no concentration quenching in Yb^{3+} occurs (energy gap between the two levels is much higher than the matrix phonons) and Yb^{3+} are known for its high absorption cross-section, the energy of Er^{3+}: $^4I_{11/2}$ level may be effectively transferred to quasi-resonant $^2F_{5/2}$ level in Yb^{3+} ion (3). This may be followed by efficient energy migration between Yb^{3+} ions and the donation from excited Yb^{3+} ions back to other Er^{3+} ions (3) like in conventional ETU upconversion process. In consequence the intermediate $^4I_{13/2}$, $^4I_{11/2}$ and $^4I_{9/2}$ levels of Er^{3+} ions should be populated aiming to increase the absorption cross section for possible ESA$_{1\text{-}7}$ processes. Eventually, these preliminary steps and Yb^{3+} sensitization[101], should potentially further enhance energy looping between Er^{3+}-Er^{3+} pairs.

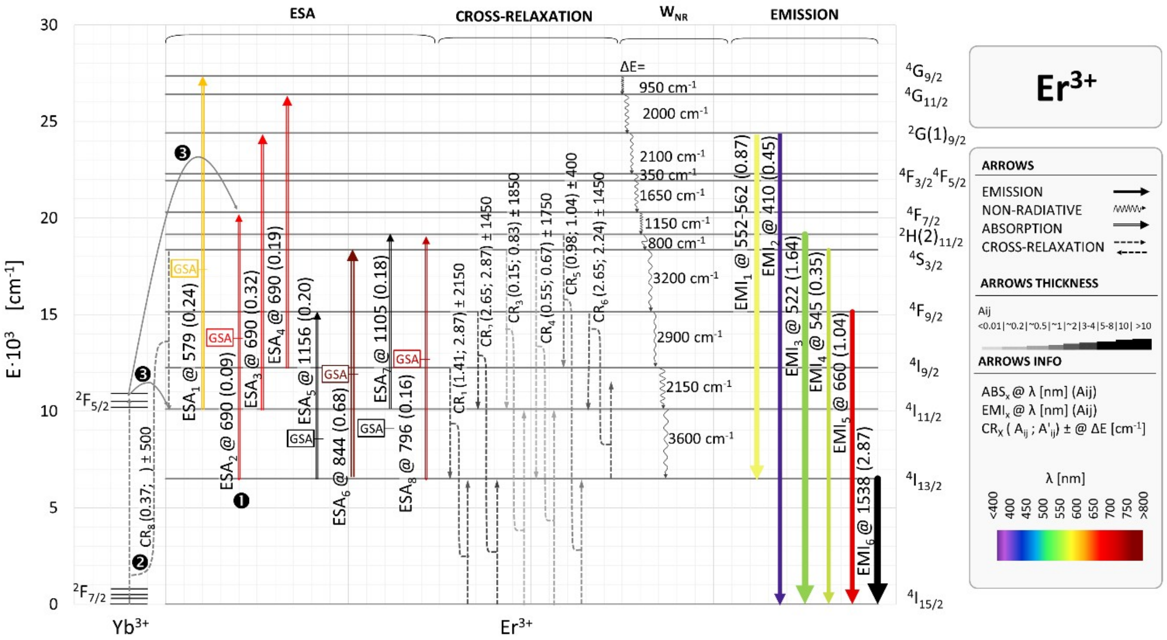

***Figure S8: Transitions and energy transfers suitable for PA** to occur in Er^{3+}.*

***Table S8: Transitions and energy transfers suitable for Er^{3+} doped materials**. $\lambda/\ \nu$ denote excitation/emission wavelength in nm/cm^{-1}; $\Delta\nu$ denotes either energy mismatch (for CR) or energy gap (for GSA,ESA,EMI) between respective levels; Data for LiYF$_4$ matrix : Ω_2=1.92; Ω_4=0.26; Ω_6=1.96^{4,4,4} A_{ij} defined by Eq.1.1. Data base on ref.* [102]

	Term	Term	λ	ν	A_{ij}	
	Start	End	[nm]	[cm^{-1}]		
Excitation						
ESA$_1$	$^4I_{11/2}$	$^4G_{9/2}$	579	17250	0.24	
ESA$_2$	$^4I_{13/2}$	$^4F_{7/2}$	690	13800	0.09	
ESA$_3$	$^4I_{11/2}$	$^2G(1)_{9/2}$	690	14300	0.32	
ESA$_4$	$^4I_{9/2}$	$^4G_{11/2}$	690	11250	0.19	
ESA$_5$	$^4I_{13/2}$	$^4F_{9/2}$	1156	8650	0.20	
ESA$_6$	$^4I_{13/2}$	$^4S_{3/2}$	844	11850	0.68	
ESA$_7$	$^4I_{11/2}$	$^2H(2)_{11/2}$	1105	9050	0.18	
ESA$_8$	$^4I_{13/2}$	$^2H(2)_{11/2}$	796	12650	0.16	
Looping				Δν		
CR$_1$	($^4I_{9/2}$; $^4I_{15/2}$)	($^4I_{13/2}$; $^4I_{13/2}$)		750	1.41; 2.87	
CR$_2$	($^4F_{9/2}$; $^4I_{15/2}$)	($^4I_{11/2}$; $^4I_{13/2}$)		1450	2.65; 2.87	
CR$_3$	($^4S_{3/2}$; $^4I_{15/2}$)	($^4I_{11/2}$; $^4I_{11/2}$)		1850	0.15; 0.83	
CR$_4$	($^4S_{3/2}$; $^4I_{15/2}$)	($^4I_{13/2}$; $^4I_{11/2}$)		1750	0.55; 0.67	
CR$_5$	($^2H_{(2)11/2}$; $^4I_{15/2}$)	($^4I_{9/2}$; $^4I_{13/2}$)		400?	0.98; 1.04	[102]
CR$_6$	($^4F_{7/2}$; $^4I_{11/2}$)	($^4I_{11/2}$; $^4F_{9/2}$)		1450	2.65; 2.24	
Emission				ν		
EMI$_1$	$^2G(1)_{9/2}$	$^4I_{13/2}$	552-562	17900	0.87	
EMI$_2$	$^2G(1)_{9/2}$	$^4I_{15/2}$	410	24400	0.45	[102]
EMI$_3$	$^2H(2)_{11/2}$	$^4I_{15/2}$	522	19150	1.64	

EMI_4	$^4S_{3/2}$	$^4I_{15/2}$	545	18350	0.35	
EMI_5	$^4F_{9/2}$	$^4I_{15/2}$	660	15150	1.04	
EMI_6	$^4I_{13/2}$	$^4I_{15/2}$	1538	6500	2.87	

1.9 Thulium ions – Tm^{3+}

Thulium ions are well-known as showing blue, red and NIR emission. Blue emission arrives from $^1D_2 \rightarrow {}^3F_4$ and $^1G_4 \rightarrow {}^3H_6$ transitions (around 455 nm and 480 nm, EMI_1 and EMI_3, respectively **Figure S9**), while NIR emission at 800 nm is observed for $^3F_4 \rightarrow {}^3H_6$ transition (EMI_5, **Figure S9**). Absorption from ground state up to $^1D_2$ level occurs at about 355 nm. Thulium ions are also one of the most investigated and most commonly used to observe PA. First demonstrations of the PA hosted on Tm^{3+} were reported mostly in low temperatures in bulk materials doped with this ion such as $LiYF_4$ crystal [103], YAP ($YAlO_3$) [104] , YAG ($Y_3Al_5O_{12}$) [105], LaF_3 YSO (Y_2SiO_5) single crystals [106], BIGaZYTZr fluoride glasses [107] , Y_2O_3 crystals [108], ZBLAN fibre [109], fluoroindate glasses [103–109] . In the most of the cases, after red or infrared photoexcitation there was observed PA blue emission at 480-486 nm and at 450 nm corresponding to $^1G_4 \rightarrow {}^3H_6$ and $^1D_2 \rightarrow {}^3F_4$ transitions , respectively. It is worth to notice that most frequently observed transition was $^1G_4 \rightarrow {}^3H_6$[104,105], nevertheless in some materials both of these transitions were obtained, for example in the case of Y_2O_3 crystal fibre [108,110] , BIGaZYTZr fluoride glasses [111], YSO (Y_2SiO_5) single crystal [106], fluoroindate glasses [111] and ZBLAN fiber [109]. In the case of $LiYF_4$ crystal, the $^1G_4 \rightarrow {}^3H_6$ emission was present at 483 nm under 628 nm excitation and $^1D_2 \rightarrow {}^3F_4$ at 450.2 nm under two-photon absorption 784.5 nm and 648 nm excitation [112–120]

For many years, the possibility to observe PA phenomenon in nanomaterials and at room temperature was questionable. In 2021 the pure PA phenomenon was observed for the first time in $NaYF_4$: Tm^{3+}@$NaYF_4$ core-shell nanoparticles, where the core, covered by passive shell, was doped with Tm^{3+} ions with various concentrations of 1%, 4%, 8%, or even as high as 20% and 100%, vitally exceeding the typically employed dopant concentrations in upconverting systems[121]. For all of the nanoparticles, excited at ambient conditions with 1064 nm light (resonant with $^3F_4 \rightarrow {}^3F_{2,3}$ ESA transition and not resonant with any GSA transition) there was observed photon avalanche emission around 800 nm (corresponding to $^3H_4 \rightarrow {}^3H_6$ transition) with high slope values exceeding 30 for nanoparticles doped with 20% of Tm^{3+}. Simultaneously, other hallmarks of PA phenomenon were observed such as emission risetime dynamics with significant slowing down for pumping power close to the PA threshold. Interestingly, 1450 nm photoexcitation, resonant with $^3F_4 \rightarrow {}^3H_4$ transition also resulted in nonlinear output, however slopes around 5 were observed. After architecture optimization (core/shell size regulation) and detailed comparison of the resulting quantum yields in broad range of applied excitation power, the 8% doped nanocrystals (slope of 26 and the PA threshold around 6 kW/cm^2) were recognized as the optimal ones for further applications and selected for super resolution imaging. It was shown, both, experimentally and with theoretical modelling, that for these nanocrystals, characterized with highly nonlinear performance, and scanned using gaussian excitation beam with appropriate power density fitted into PA regime (7.6 kW/cm^2), it was possible to take images with resolution significantly exceeding the diffraction limit (70 nm). This result is highly consistent with previously proposed approach of PA assisted super resolution imaging (PASSI) [52].

There are other well-known techniques leading to sub-diffraction imaging that are based on combining super linear excitation-emission (uSEE) and super-resolution stimulated emission depletion (STED) microscopy, where nanoparticles co-doped with Tm^{3+} (activator) and Yb^{3+}(sensitizer) can be employed [122]. Upconverting nanoparticles ($NaYF_4$:20%Yb, 8%Tm) functionalized by colominic acid were used to realize this approach.[122] Upconversion after excitation at 976 nm of Yb^{3+} ions, resulting in blue emission of Tm^{3+} ions is observed at 455 nm, which corresponds to $^1D_2$->$^3F_4$ transition. High concentration of Tm^{3+} ions provides to an efficient cross-relaxation processes, which lead to population of the excited states. This states can be also populated via non-radiative energy transitions from Yb^{3+} ions. Energy looping and avalanche-like behaviour caused by CR processes are beneficial for uSEE as well as for STED.[122] Simultaneous combination of both mentioned operations (uSEE and STED) enables to use lower laser power (2.46 MW/cm^2) than in case of single STED mode (10 MW/cm^2). Nanometer optical resolution enabling imaging of single UCNPs was obtained based on low-power super-resolution stimulated emission depletion microscopy approach.[123] The $NaYF_4$: x% Tm^{3+}, 20% Yb^{3+} (x= 1 and 8 %) nanoparticles were excited with 980 nm and then simultaneously with 980 and 808 nm wavelengths. For nanoparticles doped with 8% of Tm^{3+} ions clear decrease of blue emission from higher $^1D_2$ and $^1G_4$ levels was observed. Simultaneously NIR emission from $^3H_4$ levels was dominating. In the case of nanoparticles doped with 1% Tm^{3+} the effect of inhibiting blue emission was less visible. The essence of this phenomenon lies in CR processes, which dominate in case of small distances between emitting ions, in case of higher concentrations of emitting ions. Photon-avalanche-like behaviour was observed, which, in comparison with PA, does not show non-resonant GSA, but plays key role in stimulated emission depletion.

Recently PA phenomenon was observed in $LiYF_4$ crystals doped with 3% as well as with 8% of Tm^{3+} ions.[124] PA dependence on crystals size was investigated by analysis of bulk, micro and nano sized materials. Additionally, nanocrystals were synthesized and investigated in core and core-passive shell architectures. The experimental results were supported by theoretical model presenting, how radiative and non-radiative rates as well as cross-relaxation and ESA affect the PA phenomenon. In all the investigated materials PA was observed for emission at 800 and 475 nm. The highest slope value (12.6) was obtained for core nanocrystals with threshold around 700 kW/cm^2. It was observed, that with decrease of crystal size, thresholds shift to higher values. As a demonstration of suitability of investigated materials for photon avalanche single beam super-resolution imaging (PASSI) core-shell nanocrystals doped with 3% of Tm^{3+} ions were used and allowed to achieve spatial resolution of 125 nm.

Like discussed earlier, the energy scheme of Tm^{3+} may show some prospects for Yb^{3+} sensitization of the photon avalanche. Because Tm^{3+} , like Er^{3+} , is one of the most efficient upconverting ions, the presence of Yb^{3+} sensitizer should have important contribution in PA excitation scheme – the sequence of such sensitized PA emission was indicated on **Figure S9**. Similarly to the Yb^{3+} sensitized Er^{3+} PA emission, first, slight ESA_1 excitation (e.g. 1064 nm) would be responsible for initialization of the looping ($CR_{1,3,4}$), which then would populate the $^3F_4$, $^3H_5$, $^3H_4$ levels. Because no concentration quenching in Yb^{3+} occurs (energy gap between the two levels is much higher than the matrix phonons) and Yb^{3+} are known for its high absorption cross-section, the energy of $^3H_4$ Tm^{3+} level could be transferred to $^2F_{5/2}$ level in Yb^{3+} ions. This may be followed by efficient energy migration between Yb^{3+} ions and the Energy donation from excited Yb^{3+} ions back to other Tm^{3+} ions like in conventional ETU upconversion process. In consequence the intermediate $^3F_{2,3}$, $^1G_4$ and $^1D_2$ levels of Tm^{3+} ions can be populated, the looping $CR_{1\text{-}11}$ can be activated and absorption cross section for possible $ESA_{1\text{-}4}$ processes should be further enhanced.

Similarly as for Ho^3 ions, MPA (Migrating Photon Avalanche) was also obtained in Tm^{3+} ions, which were placed in four-layer core-shell nanoparticles: $NaYF_4$:Yb/Pr(15/0.5%)@$NaYF_4$:Yb/ Tm(3/4%) @ $NaYF_4$:Yb/Pr(15/0.5%) @ $NaLuF_4$ [31]. Excitation with 852nm caused PA looping in core of this particles, then energy was transferred to Tm^{3+} ions and PA emission was observed at 452 nm ($^1D_2 \rightarrow {}^3F_4$). To evidence, that the presence of Pr^{3+} ions is crucial for obtaining photon avalanche emission from Tm^{3+}

ions under excitation with 852 nm, Tm^{3+} as well as Tm^{3+} and Yb^{3+} co-doped particles were evaluated, which did not show any emission under this excitation.

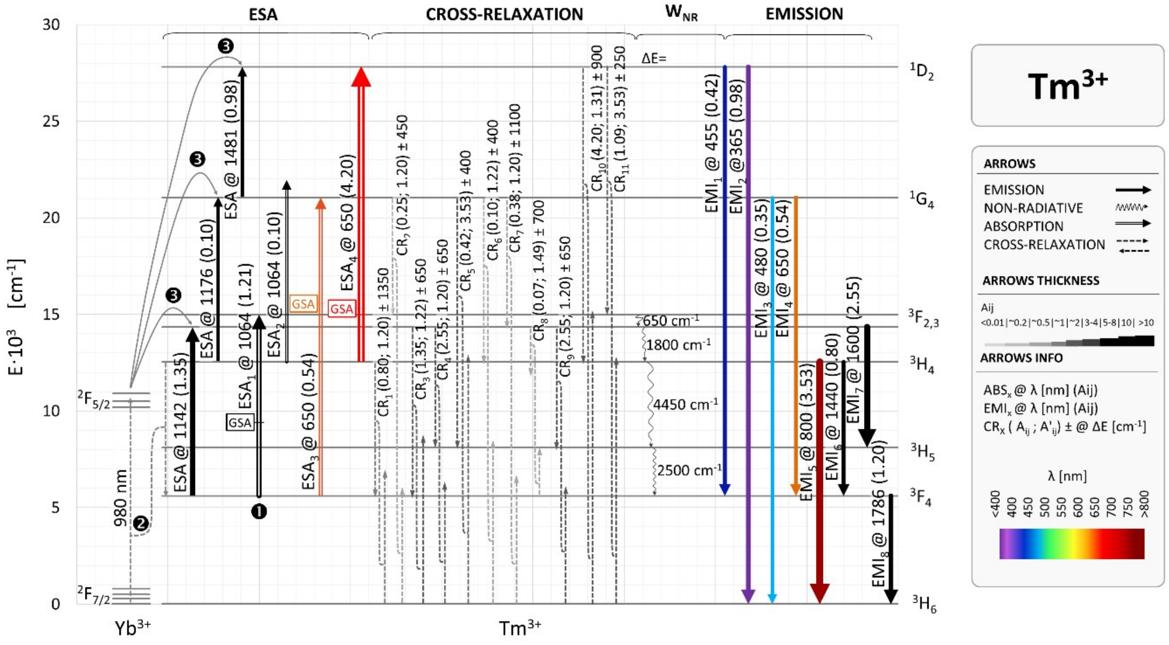

***Figure S9. Transitions and energy transfers suitable for PA** for Tm^{3+} doped materials.*

Table S9. Transitions suitable for obtaining photon avalanche in Tm^{3+} doped materials. λ/ν denote excitation/emission wavelength in nm/cm^{-1} $\Delta\nu$ denotes either energy mismatch (for CR) or energy gap (for GSA,ESA,EMI) between respective levels; Data for matrix β-$NaGdF_4$: Ω_2=2.37 Ω_4=3.05 Ω_6=0.41[125]. A_{ij} defined by Eq.1.1.

	Term Start	Term End	λ [nm]	ν [cm^{-1}]	A_{ij}	Comment
Excitation						
GSA_1	$^3H_6$	$^3H_5$	1234	8100	1.22	[126]
ESA_1	$^3F_4$	$^3F_3$	1142	8750	1.35	[121]
ESA_2	$^3H_4$	$^1G_4$	1176	8500	0.10	
ESA_3	$^1G_4$	$^1D_2$	1481	6750	0.98	[109]
ESA_4	$^3F_4$	$^3F_3$	1064	8750	1.21	
ESA_5	$^3H_4$	$^1G_4$	1064	8500	0.10	
ESA_6	$^3F_4$	$^1G_4$	650	15450	0.54	
ESA_7	$^3H_4$	$^1D_2$	650	15250	4.20	
Looping				Δν		
CR_1	($^3H_4$; $^3H_6$)	($^3F_4$; $^3F_4$)		1350	0.80; 1,20	[121,126]
CR_2	($^1G_4$; $^3H_6$)	($^3F_2$; $^3F_4$)		450	0.25; 1.20	[126]
CR_3	($^3F_3$; $^3H_6$)	($^3F_4$; $^3H_5$)		650	1.3; 1.22	

CR_4	$(^3F_3;\ ^3H_6)$	$(^3H_5;\ ^3F_4)$		650	2.55; 1.20	
CR_5	$(^1G_4;\ ^3H_6)$	$(^3H_5;\ ^3H_4)$		400	0.42; 3.53	126
CR_6	$(^1G_4;^3H_6)$	$(^3H_4;\ ^3H_5)$		400	0.10; 1.22	126
CR_7	$(^1G_4;\ ^3H_6)$	$(\ ^3F_3;\ ^3F_4)$		1100	0.38; 1.20	
CR_8	$(^3F_3;\ ^3F_4)$	$(^3H_4;\ ^3H_5)$		700	0.07; 1.49	
CR_9	$(^3F_3;\ ^3H_6)$	$(^3H_5;\ ^3F_4)$		650	2.55; 1.20	
CR_{10}	$(^1D_2;\ ^3H_6)$	$(^3H_4;\ ^3F_2)$		900	4.20; 1.31	126
CR_{11}	$(^1D_2;\ ^3H_6)$	$(^3F_2;\ ^3H_4)$		250	1.09; 3.53	
Emission				ν		
EMI_1	$^1D_2$	$^3F_4$	455	22200	0.42	31,12631,126
EMI_2	$^1D_2$	$^3H_6$	365	27800	0.98	126
EMI_3	$^1G_4$	$^3H_6$	480	21050	0.35	126
EMI_4	$^1G_4$	$^3F_4$	650	15450	0.54	126
EMI_5	$^3H_4$	$^3H_6$	800	12550	3.53	127
EMI_6	$^3H_4$	$^3F_4$	1440	6950	0.80	128
EMI_7	$^3F_3$	$^3H_5$	1600	6250	2.55	
EMI_8	$^3F_4$	$^3H_6$	1786	5600	1.20	126

In this case absorption can occurs to level $^3F_2$ or $^3F_3$. Because of it there are two values of A_{ij} respectively for absorption $^3F_4 \rightarrow {}^3F_2$ and $^3F_4 \rightarrow {}^3F_3$.

2 *Comparison of photon-avalanche and photon-avalanche-like luminescence in Ln^{3+} doped (nano) and micro-materials*

Table S10: Comparison of most representative examples of photon-avalanche and photon-avalanche-like luminescence in Ln^{3+} doped materials. *I_{TH}, I_{SAT}, S_{MAX} and $\tau_{X\%}$ respectively denote excitation power threshold and saturation (if provided), highest power dependence slope, presence of the clear PA features – power dependent risetimes with the time required to get X% of steady state emission ($\tau_{X\%}$); legend: the ☒ symbols denote missing/unavailable information, ☑ denote the feature was observed but (possibly) no numerical values were provided or were impossible to extract; NC – nanocrystals; C@S denote core-shell NPs, where size or composition may differ between core and shell; T_O – operating temperature; RT – room temperature operation. The I_{TH} and I_{SAT} are in [kW cm^{-2}], unless these numbers were provided in power units only.*

Ln^{3+} emitting dopant/s	Host & dopant	Host size	λ_{EXC} / λ_{EMI}	I_{TH} / I_{SAT}	S_{MAX}	$\tau_{x\%}$	T_O	Additional comments	Ref
			[nm/nm]	[kW/cm^2]	[n.a.]	[s]	[°C]		
Ce	$CeVO_4$	Nano 10 x 50 nm (nanoplates, nanowires, straw-sheaves)	808 / 450 – 670	☒ / ☒	7.8 (straw-sheaves)	☒	☒	No energy scheme suitable for PA. Most probably, this is relatively more efficient upconversion due to the smaller excitation threshold caused by the strong cross-relaxation between the bundled nanorods in the sheaves.	[129]
Ce	$CeVO_4$	Nano 30 nm – 40 nm square-plate	800 / 593	23 mW / …	15	☒	☒	As Ce ions are 2 level system they are unable to host PA mechanism; relation between ESA and GSA, as well as slowing down of the emission raisetime are not studied, thus observed results are difficult to be explained as PA mechanism	[130]
Pr, Yb	Pr,Yb:$YAlO_3$	Unknown size	836 nm /	☒	☒	τ_R=0.6·10^{-3}	☒	PA observed for YLF host only,	[37]

	Pr,Yb:YLF		$^3P_0 \longrightarrow ^3F_2$			$\tau_{90\%}=0.5 \cdot 10^{-3}$		no PA mechanism found in $YAlO_3$ matrix	
Pr-Yb@Yb-Tm/Ho	$NaYF_4$:Yb/Pr (15/0.5%)@ $NaYF_4$ $NaYF_4$:Yb/Pr(15/ 0.5%)@ $NaYF_4$:Yb/Ho(3/ 4%)@ $NaYF_4$:Yb/ Pr(15/0.5%)@ $NaLuF_4$ $NaYF_4$:Yb/Pr(15/ 0.5%)@$NaYF_4$:Yb/Tm(3/4%)@ $NaYF_4$:Yb/ Pr(15/0.5%)@ $NaLuF_4$	9.5-17 nm core, 2.5-4.5 nm shell	852 nm / $^1G_4 \rightarrow ^3P_0$ (Pr)/ apparently multicolor emission from Pr,Yb,Tm, Ho	~60-80 kW/cm^2 for Pr,Yb,Ho ~200 kW/cm2 for Pr/Tm	26@980 (Yb) 20@609(Pr) 28@541(Ho) 28@646(Ho) 21@484 (Pr) 46@452(Tm)	$\tau_{95\%}=19.2 \cdot 10^{-3}$ in $NaYF_4$:Yb/Pr (15/0.5%)@$NaYF_4$ nanoparticles (26 nm in diameter)	RT	Apparent multicolor (Pr,Ho,Tm PA emission overlap spectrally), photon avalanche emission of Pr:482,520,645 nm, Yb:980, Ho:540,650, Tm:455 was observed under 852nm with features characteristic for PA (high slopes, clear threshold, slow risetimes). SRI shown in-vitro.	31
Pr	Glass, glass ceramics, ceramics containing nanocrystals	Bulk 25-50 nm (calculated from XRD)	976 / Vis	1.7 mW / 2.2 mW	5.28 (@548 nm)	☒	☒	Relatively low values (less than 2) of observed slopes and lack of dynamics analysis suggest that observed results may be caused by energy looping rather than PA	131
Pr	$LaCl_3$ or $LaBr_3$ doped with 4.88% Pr^{3+}		$^3H_5(2)$ to $^3P_1(1)$ / $^3P_0$-$^3P_1$, $^3P_1$-$^3F_2$, $^3P_0$-$^3F_2$	1.2-12.2W/cm^2	☑	☒		Highly nonlinear fluorescence with pump power	132
Pr^{3+}	$NaYF_4$: 15% Yb^{3+}, 0.5% Pr^{3+}@ $NaYF_4$	NC	852/480	~60/ above 850	26	☒	RT	Mechanism of migrating photon avalanche	133
Pr, Yb	$NaYF_4$: x% Pr^{3+}, 15% Yb^{3+}@	NC cores ~ 20 nm	852/ 482 ($^3P_0$ →	Between 281 and	9 (482 nm)	$\tau_{50\%}$~5 ms for emission	RT	In this work were considered different concentration of Pr^{3+}	134

	$NaYF_4$ (x= 0.1, 0.3, 0.5, 0.7)	c@s ~ 30 nm	$^3H_4$), 607 ($^3P_0 \rightarrow {}^3H_6$)	817/ above 10^7		at 607 nm: $\tau_{80\%}$~12 ms at 482 nm: $\tau_{80\%}$: between 10 and 25 ms		ions, while Yb^{3+} concentration was constantly 15%. Additionally, the influence of inert shell on features of PA emission was investigated. The presence of inert shell, comparing with single cores, contributed to higher slopes and lower thresholds of the s-shape curve. Optimal sample, with the highest slope around 9 and the smallest PA threshold, around 281 kW/cm^2, was $NaYF_4$: 0.5% Pr^{3+}, 15% Yb^{3+} @ $NaYF_4$.	
Nd	1%Nd/5%Yb YAG	Bulk Size: ☒ NC ceramics	976 / 597	400 mW /…	5.4	$\tau_{90\%}$=$2{\cdot}10^{-3}$	RT	Hot (thermal) emission proposed to explain PA-like (slopes>2, pum-power dependent risetimes) behaviour	135
Nd	$NdVO_4$	Nano (nanoplates, nanowires, straw-sheaves) Size: 10 x 50 nm	808 / 500 – 650	☒ / ☒	14.1 (straw-sheaves)	☒	☒	Relatively more efficient upconversion due to the smaller I_{TH} caused by the strong cross-relaxation between the bundled nanorods in the sheaves. Relation between ESA and GSA, as well as slowing down of the emission risetime are not studied, thus observed results are difficult to be explained as PA mechanism	129
Nd	$NdVO_4$	Nano	800 nm /	8 mW / …	22	☒	☒	Relation between ESA and	130

		30 nm wide, 6-8 nm long (like H letter)	584 nm					GSA, as well as slowing down of the emission risetime are not studied, thus observed results are difficult to be explained as PA mechanism	
Nd	$Nd_{0.1}Y_{0.9}VO_4$ $NdVO_4$	Nano 30 x 9 nm	808 / 593, 535	90 mW / ☒@593nm 60 mW / ☒@535nm	9.5 (@593 nm) 6.7 (@535 nm)	$\tau_{90\%}=50\cdot10^{-9}$ (@535 nm)	☒	Pumping via GSA together with lack of clear evidence of luminescence risetime slowing down around the PA threshold suggest that observed results may be difficult to be explained as PA mechanism	136
Nd	Nd^{3+} doped NPs: $NaYF_4$, Y_2O_3, $YGdO_3$, $YAlO_3$, $Y_3Al_5O_{12}$, $LiLaP_4O_{12}$, Gd_2O_3	Nano 10 – 20 nm	1064 / 800	0.7 W at 10°C in $LiLaP_4O_{12}$: Nd^{3+}	☒	$\tau_{50\%}$ several milliseconds	10-200°C	anti-Stokes avalanche-like NIR emission, thresholds noticed, low slopes, rise-time kinetics not studied	55
Nd	$NdAl_3(BO_3)_4$	Nano	1064 / 810, 880	19 W/mm^2	3.7, 8.9	$10\cdot10^{-6}$	50-260 °C	Photon avalanche like upconversion	137
Nd^{3+}	KPb_2Cl_5: 16% Nd^{3+}	Nanoparticles in sizes from 8.9 nm to 155 nm depending on reaction temperature and reagents ratio (oleic acid and oleylamine)	1064/ 595 and 810	595: ~20/ ☒ 810: ~10/ ☒	~9 (@595 nm) ~12 (@810 nm)	~70 ms	RT		138
Nd^{3+}	KPb_2Cl_5: 16% Nd^{3+}	nanoparticles	1064/ 810	6.7 kW·cm-2/ ☒	200	☒	-196 °C	Low phonon energy matrix	139

Sm	$Yb_3Al_5O_{12}$ (YbAG):Ln^{3+}	Micro	980 nm / white light and IR	… / $4e^5$ mW	12.2 (white light)	☒	☒	Pumping resonantly with GSA together with lack of process dynamics analysis suggest that observed results may be difficult to be explained as PA mechanism	[140]
Eu^{3+}/Tm^{3+}	$NaGdF_4$:20% Tm^{3+} @$NaGdF_4$ @$NaGdF_4$: A^{3+} @$NaYF_4$ A^{3+} – activator, in this case Eu^{3+} ions	NC around 24 nm	1064/ ~617	~28/~48	14.6	Prolonged rise times at95% steady-state intensity depending on power densities were in the range from 40 to 90 ms.	☒	The architecture of nanomaterial contains sensitizer in core, buffer shell, activator in shell and finally protective shell.	[141]
Tb	$Yb_3Al_5O_{12}$ (YbAG):Ln^{3+}	0.27 nm	980 nm / white light	… / $1e^6$ mW	11.2	☒	☒	Pumping resonantly with GSA together with lack of process dynamics analysis suggest that observed results may be difficult to be explained as PA mechanism	[140]
Tb^{3+}/Tm^{3+}	$NaGdF_4$:20% Tm^{3+} @$NaGdF_4$ @$NaGdF_4$: A^{3+} @$NaYF_4$ A^{3+} – activator, in this case Tb^{3+} ions	NC around 24 nm	1064/ ~546	~170/~214	17.2	Prolonged rise times at95% steady-state intensity depending on power densities were in the range from	☒	The architecture of nanomaterial contains sensitizer in core, buffer shell, activator in shell and finally protective shell.	[141]

						40 to 90 ms.			
Ho	Ho^{3+} –Yb^{3+} co-doped glass–ceramics containing CaF_2 nanocrystals	8, 10, 13, 18 nm	745 / 545, 650	0.410 /☒	3.1	$\tau_{90\%}$ from 18 to 33 ·10^{-3}	RT	Despite pumping resonantly with ESA transition and well-evidenced slowing down of the luminescence rising times, rather low slope values suggest that this phenomenon should be explained by energy looping than PA	142
Ho	1Ho:$Lu_3Ga_5O_{12}$ 1Ho:$Y_3Ga_5O_{12}$	Nano 50-90 nm	751 / 545	0.331 / ☒ 0.238 / ☒	2.54 2.14	☒	☒	Despite pumping resonantly with ESA transition and well-evidenced slowing down of the luminescence rising times, rather low slope values suggest that this phenomenon should be explained by energy looping than PA	143
Ho	$Ho_{0.5}$:Gd_2O_3 $Ho_{0.5}$:Yb_3:Gd_2O_3 Annealed $Ho_{0.5}$:Yb_3:Gd_2O_3	Nano ~100 nm	976 / 553, 669	150 / 350 mW	4.8 @553, 4.5@669	$\tau_{90\%}$=0.005@ 553 nm	☒	Despite evidenced slowing down of the luminescence rising times, rather low slope values suggest that this phenomenon should be explained by energy looping than PA. Moreover, other mechanisms, such as ETU, are also present in considered system.	144
Ho^{3+}/Tm^{3+}	$NaYF_4$: 8% Tm^{3+}@$NaYF_4$: 1%Ho^{3+} @$NaYF_4$ $NaYF_4$: 3% Tm^{3+}@$NaYF_4$:	NC	1064/ Ho^{3+}: 646 and 542 Tm^{3+}: 800	10.5/~40	Ho^{3+}: 17 (646 nm) 15 (542 nm) Tm^{3+}: 14 (800 nm)	For different Er^{3+} ions concentrations all emissions of Tm^{3+} and Er^{3+} presented elongated	☒	Ho^{3+} ions were excited by interfacial energy transfer between these and Tm^{3+} ions.	145

	1%Ho^{3+}@$NaYF_4$ $NaYF_4$: 8% Tm^{3+}, 0.2% Ho^{3+}@ $NaYF_4$				Ho^{3+}: 18 (646 nm) 19 (542 nm) Tm^{3+}: 16 (800 nm) Ho^{3+}: 8 (646 nm) 6 (542 nm) Tm^{3+}: 5 (800 nm)	risetimes from 0.6 to 1.1 s.			
Ho^{3+}/Tm^{3+}	$NaGdF_4$:20% Tm^{3+} @$NaGdF_4$ @$NaGdF_4$: A^{3+} @$NaYF_4$ A^{3+} – activator, in this case Ho^{3+} ions	NC around 24 nm	1064/ ~646	9/~21	11.5	Prolonged rise times at95% steady-state intensity depending on power densities were in the range from 40 to 90 ms.	☒	The architecture of nanomaterial contains sensitizer in core, buffer shell, activator in shell and finally protective shell.	141
Er	Glass (glass-ceramics, ceramics containing nano-crystals of different phases doped with Er^{3+}/Yb^{3+} ions)	40nm	976 nm / 410, 534, 556, 672nm 532 nm / 387, 410, 458, 491 nm	c.a. $10^{1.6}$ mW / $10^{2.0}$ mW c.a. $10^{2.25}$ mW / above $10^{3.25}$ mW	(ex 976 nm) 8.87 @556nm (ex532nm) 1.84 @491nm	☒	RT	GSA / ET / ESA	146
Er	$Yb_3Al_5O_{12}$	Micro	980 nm /	… below	11.8	☒	☒	Pumping resonantly with GSA	140

	(YbAG):Ln^{3+}		white light	e^6 mW/ $4e^7$ mW				together with lack of process dynamics analysis suggest that observed results may be difficult to be explained as PA mechanism	
Er	KLa5%ErYb P_4O_{12} La5%ErYbP_5O_{14}	Nano 30 nm	980 / 548, 650	1W /☒ 0.6W /☒	1.5 - 3.5 (@545); 1- 4 (@654)	☒	☒	Yb concentration affects emission intensity	147,148
Er	Yb^{3+}, Er^{3+} : KLu_2F_7 NPs	Nano/Micro 100 nm to 2 µm	377 + 980 / UV, IR	2.7 mW / ☒	3.69	☒	RT	2Ph process (for 980 nm) For dual excitation quasi-photon avalanche (QPA) mechanism is proposed	149
Er, Li	Er / (0,5,10%) Li co-doped BiOCl	Micro 1 to 2 µm	980 / ~540, ~650	0.070 / ☒	8.30 (5%Li) @540 7.33 (0%Li) @650	☒	☒	Pumping resonantly with GSA together with lack of process dynamics analysis and rather low slope values suggest that observed results may be difficult to be explained as PA mechanism	150
Er	$Gd_2O_{3-x}S_x$:Er	Nano 53.7, 47.5, 47.2 and 49.1 nm	978 / 671, 549	☒ / ☒	☒	☒	☒	Lack of process dynamics analysis suggest that observed results may be difficult to be explained as PA mechanism Short rise times (below 250 µs)	151
Er	BiOCl:Er^{3+}	Nano 150, 70, 35 nm Nanosheets	980 / 540, 650	0.085 / ☒	7.86 (red emission, pH6)	$\tau_R = 33 \cdot 10^{-3}$ $\tau_{90\%} = 19 \cdot 10^{-3}$	☒	Lack of process dynamics analysis and rather low slope values suggest that observed results may be difficult to be explained as PA mechanism	152
Er^{3+} / Yb^{3+}	$NaBi(WO_4)_2$: 1% Er^{3+} 7% Yb^{3+}	Nano 53 nm	980 / 523, 548	300 / 175 mW	8.4, 6.6	τ_R between 200 and $500 \cdot 10^{-6}$	RT	Pumping GSA of Yb^{3+}, but slope equals around 6-9, risetimes are slightly longer than	148

						$\tau_{90\%}$ at 1500 $\cdot 10^{-6}$		upconversion (rather comparable to upconversion or looping)	
Er^{3+}	BiOCl: Er^{3+}	Nano	980 / 550, 650 1560	70 / 90 Wcm^{-2}	6.51 / ☑ / ☑	☒	☒	Energy looping	153
Er^{3+}	$Bi_9V_2O_{18}Cl$: $0.5Er^{3+}$ / $5Er^{3+}$			0.12 / ☒	1.29-3.86	☒	☒	Multi-photon	154
Er^{3+}/ Tm^{3+}	$NaYF_4$:8%Tm^{3+}@ $NaYF_4$@1%Er^{3+} $NaYF_4$:8%Tm^{3+}@ $NaYF_4$@1%Er^{3+} @$NaYF_4$ $NaYF_4$:8%Tm^{3+}@ $NaYF_4$@5%Er^{3+} @$NaYF_4$	NC around 30 nm (cores 20.7 nm)	1064/ Er^{3+}: 655 and 542 Tm^{3+}: 800	18-22/ ~40	Er^{3+}: 16 (655 nm) 19 (542 nm) Tm^{3+}: 15 (800 nm) Er^{3+}: 19 (655 nm) 21 (542 nm) Tm^{3+}: 16 (800 nm) Er^{3+}: 20 (655 nm) 23 (542 nm) Tm^{3+}: 18 (800 nm)	For different Er^{3+} ions concentrations all emissions of Tm^{3+} and Er^{3+} presented elongated risetimes from 0.6 to 1.1 s.	☒	The Tm^{3+} ions were excited by 1064 nm. Er^{3+} ions were excited by interfacial energy transfer (IET) from Tm^{3+} ions.	145
Er^{3+}/ Tm^{3+}/Ce^{3+}	$NaYF_4$:8%Tm^{3+}@ $NaYF_4$@5%Er^{3+} @$NaYF_4$: 5% Er^{3+}, 5% Ce^{3+}	NC	1064/ Er^{3+}: 655 and 540 Tm^{3+}: 800	7.1/~20	Er^{3+}: 41 (540 nm) 39 (655 nm) Tm^{3+}: (800 nm)	For different Er^{3+} ions concentrations all emissions of Tm^{3+} and Er^{3+} presented elongated risetimes from 0.6 to 1.1 s.	☒	Tm^{3+} ions are excited and occurs the interfacial energy transfer (IET). Ce^{3+} ions facilitate population of reservoir energy level, therefore the nonlinearity of Er^{3+} ions emission is enhanced.	145

Er^{3+}/Tm^{3+}	$NaGdF_4$:20% Tm^{3+} @$NaGdF_4$ @$NaGdF_4$: A^{3+} @$NaYF_4$ A^{3+} – activator, in this case Er^{3+} ions	NC around 24 nm	1064/ ~660	7/above 18	10.7	Prolonged rise times at95% steady-state intensity depending on power densities were in the range from 40 to 90 ms.	☒	The architecture of nanomaterial contains sensitizer in core, buffer shell, activator in shell and finally protective shell.	141
Tm	$NaYF_4$:x%Tm20 %Gd (x=0.1 to 1.5)	Nano 40 nm	1064 / 800	~1.6 mW / ~2.0 mW	3.2	☒	☒	Although excitation is well fitted to ESA, it is also well fitted to GSA. This fact, combined with lack of the process dynamics suggest that observed results may be difficult to explain as PA mechanism	155
Tm^{3+}	β-$NaYF_4$: Tm^{3+}@ $NaY_{0.8}Gd_{0.2}F_4$	NC c@s~30 nm	1064 and 400~840/ 800	~10/above 50 (before photodarkening) ~43/above 150 (after photodarkening)	☒	☒	20-120	Individual nanoparticles were investigated.	156
Tm	$NaYF_4$:20% Gd^{3+}, 0.1-1.5 %Tm^{3+}	Nano 10 nm	1064 / 800	10^4 / 10^5	3.2	☒	☒		157

Tm	Yb/Tm co-doped NaYF$_4$ UCNPs 20% Yb 0.5%-8% Tm	Nano 40nm	980, 980 + 808 / 455	☒ /Decreases with increase of Tm^{3+}dopant from 71.4 MW/cm^2 to 0.19 MW/cm^2.	For 8%: ☒/~1ms/ ~0.41ms For 1%: ☒/~1.5ms/ ~0.9ms	For 8%: $\tau_R \sim 1\cdot10^{-3}$ $\tau_{90\%} \sim 0.41\cdot10^{-3}$ For 1%: $\tau_R \sim 1.5\cdot10^{-3}$ $\tau_{90\%} \sim 0.9\cdot10^{-3}$	RT	After adding excitation wavelength at 808 nm, emission at 455 nm, which for single excitation at 980 nm was previously observed is inhibited. Principle of non-resonant absorption from ground state is not fulfilled. However cross-relaxation processes are present and dominates for higher concentration of dopant Tm^{3+} ions.	123
Tm	NaYF$_4$: 20% Yb, 8% Tm	Nano 46 nm	976 / 455	100/250	6.2	☒	☒	super-linear emitters, 3D sub-diffraction imaging	158
Tm	NaYF$_4$: 20% Yb, 8% Tm	Nano 46 nm	976 (exc) + 808 (dep) / 455	60 / 90 @455 nm	6.4	☒	☒	Simultaneous super-linear excitation-emission and emission depletion Emission intensity of 455 nm drops above 8 times after using two excitation sources (976 nm + 808 nm)	122
Tm	NaY$_{0.99}$Tm$_{0.01}$F$_4$	microsphere blanked with nanoplates of fluorides 5 µm	1064 / ~800	~0.6 / 2	4.9 (ELNP-PS microsphere resonators) 5.5-6.1 (hexagonal nanoplates (250 × 120 nm))	☒	☒	Low-Threshold Micro lasers	159
Tm	NaYF$_4$: 20% Yb^{3+},	Nano	976 / 800	1 – 1000	☑	☒	☒	Upconversion Nonlinear	160

	x% Tm^{3+} NPs, x = 0.5- 8 $NaYF_4$: x% Yb^{3+}, 4% Tm^{3+} NPs, x = 20-80	~20 nm		/ 100 – 10000				Structured Illumination Microscopy Value of pump power density of threshold as well as slope increase with Tm^{3+} concentration.	
Tm	β-$NaYF_4$ @ β-$NaYF_4$ 8% Tm@…	Nano Size: 17@5.6nm	1064 / 800; 1450 / 800	6 / 8 35 / 45	26 / ☑ 14.3	$\tau_{90\%}$=0.6 $\tau_{95\%}$=0.608	RT	I_{TH},S_{MAX} varied with dopant concentration, shell thickness and λ_{EXC}; First demo of super-resolution imaging with PASSI	161
Tm	$LiYF_4$: 3% Tm^{3+}@ $LiYF_4$ $LiYF_4$: 8%Tm^{3+} @ $LiYF_4$	Nanoparticles: core 23-31 nm, core-shell 38-50 nm; Microparticles: 23-61 µm; Bulk crystal: ~3 mm	1059/800 1059/475	3%Tm: Nano core: 700-800/2200 Nano core-shell: 700-800/2500 Micro: 300-400 / 1800 Bulk: 200/ 1400 8% Tm^{3+}: Nano core: 2200/4500 Nano cor-shell: 1300/300	12.6	$t_{50\%}$: 9.4 for nano 3%Tm core, 36 for nano 3%Tm core-shell, 53.7 for 3%Tm microcrystals, 122 for 3% bulk; 1.9 for nano 8%Tm core, 18 nano 8%Tm core-shell, 7.6 for 8%Tm microcrystals	RT	Maximum slope value was obtained for core nanoparticles doped with 3% of Tm^{3+} ions. Values of I_{TH}, I_{SAT}, S_{MAX} and $\tau_{50\%}$ are given for emission at 800 nm.	124

				0 Micro: 300/ 3100					
Tm^{3+}	$NaGdF_4$: Tm^{3+} @$NaGdF_4$	NC ANPs+QD	1064/ Tm: 800 1064/ QD: 630	Tm:~30 QD: ~70/ Tm: above 77 QD: above 155	15.2	Prolonged rise times at95% steady-state intensity depending on power densities were in the range from 40 to 90 ms.	☒	The Tm^{3+} doped nanocrystals showing PA emission were used also to activate PA emission of quantum dots.	141
Tm^{3+}	$KMgF_3$:5% Tm^{3+}	From 12.2±1.1 nm to 30.8±1.2 nm depending on reaction time and temperature	1064/802	16.6/above 37	27	$T_{95\%}$=281 ms	RT		162
Yb	Gd_2O_3: 25 mol % Yb^{3+}	Nano diameter ~46.5 nm, length ~381.9 nm	980 / white emission	600 / 1200 mW	☒	τ_R=1.21 $\cdot 10^{-3}$ for the power 0.53 W τ_R=14.13 $\cdot 10^{-3}$ for the power 1.51 W	RT	Lifetime changes dependent on excitation power	163
Yb^{3+}/Tm^{3+}	$NaYF_4$:8%Tm^{3+}@ $NaYF_4$@5%Er^{3+} @$NaYF_4$:10%	NC	1064/980	22.5/ ~30	14	For different Er^{3+} ions concentrations all emissions	☒		145

	Yb^{3+}					of Tm^{3+} and Er^{3+} presented elongated risetimes from 0.6 to 1.1 s.			
$Tm^{3+} \rightarrow Tm^{3+}$+ Yb^{3+}+Gd^{3+} → Gd^{3+} - Tb^{3+}/ Eu^{3+}/ Dy^{3+}/ Nd^{3+} Tm^{3+}+ Yb^{3+}+Ho^{3+}	C-S-S $NaGdF_4$ NPs	NC	1064	100-150	60	☒	☒	Spectra overlap between ‘workhorse Tm ions, and emitting ions	[176]

3 Collection of studies on super resolution imaging with lanthanide doped nanoparticles

Table S11: Up-to-date studies on super resolution imaging with lanthanide doped nanoparticles. STED - super-resolution stimulated emission depletion microscopy, NL – labels exhibiting non-linear luminescence (e.g. 2,3,4,… photon upconversion; uSEE - super-linear excitation-emission; PASSI – Photon avalanche single beam super-resolution imaging); NSI - nonlinear structured illumination microscopy, SAT – saturation nanoscopy (FED - Fluorescence emission difference / near-infrared emission saturation (NIRES) nanoscopy/ NIR Bessel-beam emission saturation nanoscopy); CW= continuous wave; qCW – quasi continuous wave (i.e. 80MHz); image acquisition: RS- raster scanning, SIM – Structured Illumination Microscopy; * it is not always possible to derive resolution based on provided data (ϕ – denotes the diameter [nm] of the single NPs used), ** for STED experiments the standard excitation and depletion beam intensity is provided (the numbers without units denote kW/cm^2)

Dopants	Host	Technique	I_{EXC}/I_{DEP} [kW/cm^2]**	$\lambda_{EXC}/\ \lambda_{DEP}/\ \lambda_{EMI}$ [nm]	Resolution*	Comments	reference
1%Pr	YAG	Pulsed STED	5 Mw / 1.3 μs 25 mW	690/532/<450nm	ϕ = 32 → 50nm, RS	UV emission through f-d depletion and 532 nm probing	R.Koleshov et al.[164] (2011)
2%Yb:2%Er (2hv) 6%Yb:1%Tm (3hv) 12%Yb:0.5%Tm (4hv)	KY_3F_{10} (2hv) LaF3 (3hv) KY_3F_{10} (3hv)	CW NL	20 μW 30 μW 5 μW	980/../540 (2hv) 980/../470 (3hv) 980/../450 (4hv)	ϕ = 20-50 nm → 297/239/190 (for 2/3/4 hν), RS	2,3,4 photon upconversion	Caillat et al. (2013)[165]
1%Tm:1%Nd:30%Yb @20%Nd	$NaYF_4$@$NaYF_4$	CW NL	3.6 (2hv) 35 (3-4hv)	730/../650 (2hv) 980/../474 (3hv) 980/../455 (4hv)	ϕ = 30 nm 250/185 /168 (with 2/3/4 hν), RS	2,3,4 photon upconversion	B.Wang et al., (2016)[166]
60%Yb2%Tm	NaYF4	He Ion-beam		1.265eV(~980nm)/../800	< 30 nm 28 nm, RS	Emission stable >66min, visualization of NP in HeLa cells	Z.Mi et al., (2015)[167]
20%Yb 8%Tm	β-NaYF4	CW STED	1 mW/5-40 mW = 660/980 nm	980/808/455	12.9 nm → ~32 nm, RS	High photostability demonstrated >30 min @10MW/cm^2	Y.Liu et al. (2017) [123]
Tm^{3+}	β-$NaYF_4$	Confocal	For	1064, 700/☒	Below 70 nm	Thick layer (5 μm) of	[156]

		microscopy was used to image photon avalanching nanoparticles	darkening (1064 nm): 435 For photo brightening (700 nm): 164	/800		8%Tm^{3+} avalanching nanoparticles was investigated to check, if photo switching can be applied for high-density patterning applications. There were prepared 2D and 3D patterns.	
Tm^{3+}	β-NaYF$_4$	indefinite NIR PA localization microscopy (INPALM)	for 1064 nm: 33.8 for imaging 267 for photodarkening For 532 nm: 842 for photo brightening	1064, 532/☒ /800	Localization accuracy < 1 Å	The INPAM was used to determine, how indefinite ANP photo switching impacts localization accuracies in super-resolution microscopy techniques. Individual nanoparticles and clusters were imaged.	156
1%Nd:10%Yb:0.5%Er @ 20%Nd	β-NaYF4	CW SAT(FED)	10000 (solid) /10000 (doughnut)	808/808/650	ϕ = 38nm → 80 nm, RS	Solid and doughnut beams @ 808nm	Q.Wu et al. (2017)[168]
18Yb10Tm (f=18nm) 40Yb10Tm@15Tb (f=28nm)	β-NaYF4	CW STED	700/17700	975/810/455(Tm) or 547(Tb)	ϕ = 18 nm → 66 nm (82 nm in-vitro), RS	Visualisation of cellular cytoskeleton protein desmin, two colour (Tm@455 and Tb@546 STED demonstrated)	Q.Zhan et al. (2017) [169]
20% Yb, 4% Tm	β-NaYF4	CW SAT(NIRES)	4000	980 (doughnut)/…/800	ϕ = 40 → < 50 nm (δ = 33.9 nm), RS	Achieved also at 93 mm depths in thick tissue samples	C.Chen et al. (2018)[170]

...@90%Yb10%Tm	β-NaYF4@ β-NaYF4	CW STED	77/ ☒	975/810/455	ϕ = 29 nm (δ = 72nm), RS	10μs dwell time	X.Peng et al. (2019)[171]
Nd	–	CW NL (PASSI)		1064/-/860	δ_{TH} < 25 nm,RS	Conceptual work, theoretical S_{TH} up to 80, discussion on Nd, but applicable to any PA nanoparticles	A.Bednarkiewicz et.al.[52] (Mar2019)
20%Yb8%Tm	β-NaYF4	CW NL (uSEE)	1200	976/ ☒ /455	ϕ = 46 → 202nm(δ_{XY} =210 nm / δ_z ~ 450 nm), RS	Non-linear S=6.2, 3D sub-diffraction microscopy imaging in neuronal cells	D.Denkova et al. (Jul2019)[158]
3%Dy	β-NaYF4	qCW STED	2000 / 320000	452,473/748/575	ϕ = 25.4 → 89 nm, RS		S.Krause et al. (2019)[172]
3%Eu	β-NaYF4	qCW STED	670 / 222000	465/695/532-633	ϕ = 15.8 → 130 nm, RS	96% depletion efficiency at 222 MW/cm^2	S.Krause et al. (2019)[172]
40% Yb , 4% Tm	β-NaYF4	CW SAT(NIRB)	8900	980 (doughnut)/…/800	ϕ = 88 → 78 nm (δ= 98 nm), RS	Achieved in 3D at c.a. 56 mm inside spheroids	H.Liu et al. (2020)[173]
40% Yb, 4% Tm	β-NaYF4	CW SIM	10	980 (x-y sin pattern)/…/800	ϕ = 40 nm → < 130 nm (δ=130nm) 8x8 μm^2, 1 fps, 25 raw frames	wide-field super-resolution imaging within biological transparent window	B.Liu et al. (2020)[174]
20%Yb8%Tm	β-NaYF4	CW STED+NL (uSEE)	5500 uSEE 5500 / 9400 uSEE + STED	976 / ☒ / 455 uSEE 976 / 808 / 455 STED	$\delta xy/\delta z$ = 248/599 (uSEE) $\delta xy/\delta z$=132/683 (STED) $\delta xy/\delta z$=79/502 (uSEE+STED), RS	S=6.4, STED+uSEE used jointly, also in neuron phenotype cells	M.Plöschner et al. (2020)[122]
8%Tm/…	β-NaYF4@β-NaYF4	CW NL (PASSI)	7.6 / -	1064 / - / 800	ϕ < 30 nm → < 80 nm, RS	First experimental demonstration of pure single beam photon	C. Lee [161]

						avalanche (slopes >20) nanoparticles for RS super-resolution imaging	
15%Yb,0.5%Pr	β-NaYF4	Single-NIR-CW-beam super resolution imaging	828-76/	852/ ☒ / Vis (Pr 484/520/645; Ho 540/650; Tm 475) and NIR (Yb)	ϕ =26 nm	Super resolution imaging with nanoparticles showing PA emission with slope above 20.	[31]
Pr^{3+}, Yb^{3+}, Tm^{3+}	$NaYF_4$, $NaGdF_4$	3D highly-nonlinear super-resolution microscopy	70 (theoretical model) Experiment: 129 (Pr^{3+} @ 484 nm) 245 (Tm^{3+} @ 452 nm) 142 (Pr^{3+} @ 609 nm) 232 (Tb^{3+}@550 nm)	852/☒/Pr^{3+}:484, 609; Tm^{3+}452, Tb^{3+} 550	~58 nm (theoretical model) FWHM=83 nm(@484 nm) FWHM=76 nm(@452 nm) FWHM=169 nm(@609 nm) FWHM=111 nm(@550 nm)	Super resolution microscopy based on theoretical calculations and experimental investigations	[133]
Pr^{3+}, Yb^{3+}, $Tm^{3+} \rightarrow Gd^{3+}$ - Tb^{3+}/Eu^{3+}	$NaYF_4$, $NaGdF_4$	Multi-colour sub-diffraction	~300 kWcm^{-2}	852/☒/Pr^{3+}:484, 609; Tm^{3+}452, Tb^{3+} 550 / Eu^{3+} 620	107 nm @605, 120 nm@440, 108 nm @550 nm spectral chanells	3 spectral channels	[175]

		imaging					
Pr^{3+}, Yb^{3+}, Tm$^{3+}\rightarrow$Gd^{3+} - Tb^{3+}	NaYF$_4$	2 colour sub-diffraction imaging		852/☒/Pr^{3+}:484 +452 nm; 609+550nm	58 nm @ 70 kWcm^{-2} 76-85 nm @ 130-250kWcm^{-2} @ 452/484 nm 111-169 nm @142-232 kW cm^{-2}@ 609/550 nm	3D 2 spectral channels, both axial and horizonal analysis	[133]

4 References

1. Guy, S., Joubert, M. F. & Jacquier, B. Photon avalanche and the mean-field approximation. *Phys Rev B* **55**, 8240–8248 (1997).
2. Joubert, M. F., Guy, S. & Jacquier, B. Model of the photon-avalanche effect. *Phys Rev B* **48**, 10031–10037 (1993).
3. Joubert, M. F. Photon avalanche upconversion in rare earth laser materials. *Opt Mater (Amst)* **11**, 181–203 (1999).
4. Kaminskii, A. A. *Crystalline Lasers : Physical Processes and Operating Schemes*. (CRC Press, Boca Raton, 1996).
5. Renfro, G. M., Windscheif, J. C., Sibley, W. A. & Belt, R. F. Optical transitions of Pr3+ and Er3+ ions in LiYF4. *J Lumin* (1980) doi:10.1016/0022-2313(80)90045-9.
6. Adam, J. L., Sibley, W. A. & Gabbe, D. R. Optical absorption and emission of LiYF4:Pr3+. *J Lumin* **33**, 391–407 (1985).
7. Lawson, J. K. & Payne, S. A. Excited-state absorption of Pr3+-doped fluoride crystals. *Opt Mater (Amst)* (1993) doi:10.1016/0925-3467(93)90018-V.
8. Eyal, M., Greenberg, E., Reisfeld, R. & Spector, N. Spectroscopy of praseodymium(III) in zirconium fluoride glass. *Chem Phys Lett* **117**, 108–114 (1985).
9. Nakamura, I., Yoshihiro, T., Inagawa, H., Fujiyoshi, S. & Matsushita, M. Spectroscopy of single Pr 31 ion in LaF 3 crystal at 1.5 K. doi:10.1038/srep07364.
10. Remillieux, A. *et al.* Upconversion mechanisms of a praseodymium-doped fluoride fibre amplifier. *J Phys D Appl Phys* (1996) doi:10.1088/0022-3727/29/4/004.
11. Pandey, A. & Rai, V. K. Pr3+-Yb3+ codoped Y2O3 phosphor for display devices. *Mater Res Bull* **57**, 156–161 (2014).
12. Xu, B., Camy, P., Doualan, J.-L., Cai, Z. & Moncorgé, R. Visible laser operation of Pr^3+-doped fluoride crystals pumped by a 469 nm blue laser. *Opt Express* (2011) doi:10.1364/oe.19.001191.
13. Sandrock, T., Scheife, H., Heumann, E. & Huber, G. High-power continuous-wave upconversion fiber laser at room temperature. *Opt Lett* (1997) doi:10.1364/ol.22.000808.
14. Smart, R. G. *et al.* CW room temperature operation of praseodymium-doped fluorozirconate glass fibre lasers in the blue-green, green and red spectral regions. *Opt Commun* **86**, 333–340 (1991).
15. Xie, P. & Gosnell, T. R. Room-temperature upconversion fiber laser tunable in the red, orange, green, and blue spectral regions. *Opt Lett* **20**, 1014 (1995).
16. Rai, V. K. *et al.* Surface-plasmon-enhanced frequency upconversion in Pr3+ doped tellurium-oxide glasses containing silver nanoparticles. *J Appl Phys* (2008) doi:10.1063/1.2919566.
17. Golovynskyi, S. *et al.* Optical windows for head tissues in near-infrared and short-wave infrared regions: Approaching transcranial light applications. *J Biophotonics* **11**, e201800141 (2018).

18. Milojkov, D. V. *et al.* Fabrication and characterization of luminescent Pr3+ doped fluorapatite nanocrystals as bioimaging contrast agents. *J Lumin* **217**, 116757 (2020).

19. Xiong, P., Peng, M., Qin, K., Xu, F. & Xu, X. Visible to Near-Infrared Persistent Luminescence and Mechanoluminescence from Pr $^{3+}$ -Doped LiGa $_5$ O $_8$ for Energy Storage and Bioimaging. *Adv Opt Mater* **7**, 1901107 (2019).

20. Espinoza, S. *et al.* Characterization of Micro- and Nanoscale LuPO $_4$:Pr $^{3+}$,Nd $^{3+}$ with Strong UV-C Emission to Reduce X-Ray Doses in Radiation Therapy. *Particle & Particle Systems Characterization* **36**, 1900280 (2019).

21. Popovich, K. *et al.* LuAG:Pr3+-porphyrin based nanohybrid system for singlet oxygen production: Toward the next generation of PDTX drugs. *J Photochem Photobiol B* **179**, 149–155 (2018).

22. Osiac, E. *et al.* Orange and red upconversion laser pumped by an avalanche mechanism in Pr3+, Yb3+:BaY2F8. *Appl Phys Lett* (2003) doi:10.1063/1.1579561.

23. Babu, P. & Jayasankar, C. K. Spectroscopy of Pr3+ ions in lithium borate and lithium fluoroborate glasses. *Physica B Condens Matter* (2001) doi:10.1016/S0921-4526(01)00239-3.

24. Yin, M., Krupa, J. C., Antic-Fidancev, E., Makhov, V. N. & Khaidukov, N. M. Excitation spectroscopy of K2YF5:Pr3+ crystals. *J Lumin* (2003) doi:10.1016/S0022-2313(02)00391-5.

25. Shaw, L., Harbison, B., Cole, B., Sanghera, J. & Aggarwal, I. Spectroscopy of the IR transitions in Pr3+ doped heavy metal selenide glasses. *Opt Express* (1997) doi:10.1364/oe.1.000087.

26. Durteste, Y., Monerie, M., Allain, J. Y. & Poignant, F. Amplification and lasing at 1·3μm in praseodymium-doped fluorozirconate fibres. *Electron Lett* **27**, 626–628 (1991).

27. Allain, J. Y., Monerie, M. & Poignant, H. Red Upconversion Yb-Sensitised Pr Fluoride Fibre Laser Pumped In 0.8μm Region. *Electron Lett* (1991) doi:10.1049/el:19910721.

28. Garapon, C., Malinowski, M., Joubert, M. F., Kaminskii, A. A. & Jacquier, B. IR luminescence from the 1G4 multiplet of Pr3+ in various doped crystals. *Journal De Physique* (1994) doi:10.1051/jp4:1994483.

29. Sandrock, T., Heumann, E., Huber, G. & Chai, B. H. T. *OSA Trends in Optics and Photonics on Advanced Solid State Lasers*. vol. 1 (Optical Society of America, Washington DC, 1996).

30. Kück, S. *et al.* Avalanche up-conversion processes in Pr, Yb-doped materials. *J Alloys Compd* **300**, 65–70 (2000).

31. Liang, Y. *et al.* Migrating photon avalanche in different emitters at the nanoscale enables 46th-order optical nonlinearity. *Nature Nanotechnology 2022* 1–7 (2022) doi:10.1038/s41565-022-01101-8.

32. Chivian, J. S., Case, W. E. & Eden, D. D. The photon avalanche: A new phenomenon in Pr3+-based infrared quantum counters. *Appl Phys Lett* **35**, 124–125 (1979).

33. Kueny, A. W., Case, W. E. & Koch, M. E. Nonlinear-optical absorption through photon avalanche. *Journal of the Optical Society of America B* **6**, 639 (1989).

34. Gatch, D. B., Holmstrom, S. A. & Yen, W. M. Photon avalanche in Pr3+ : LaCl3. *J Lumin* **83–84**, 55–59 (1999).

35. Koch, M. E., Kueny, A. W. & Case, W. E. Photon avalanche upconversion laser at 644 nm. *Appl Phys Lett* **56**, 1083–1085 (1990).

36. Gomes, A. S. L., Maciel, G. S., de Araújo, R. E., Acioli, L. H. & de Araújo, C. B. Diode pumped avalanche upconversion in Pr3+-doped fibers. *Opt Commun* **103**, 361–364 (1993).

37. Kück, S. *et al.* Avalanche up-conversion processes in Pr, Yb-doped materials. *J Alloys Compd* **300–301**, 65–70 (2000).

38. Mishra, K., Dwivedi, Y. & Rai, S. B. Observation of avalanche upconversion emission in Pr:Y 2O 3 nanocrystals on excitation with 532 nm radiation. *Appl Phys B* **106**, 101–105 (2012).

39. Osiac, E. *et al.* Spectroscopic characterisation of the upconversion avalanche mechanism in Pr3+,Yb3+:BaY2F8. *Opt Mater (Amst)* (2003) doi:10.1016/S0925-3467(03)00089-2.

40. Kaminskiĭ, A. Aleksandrovich. *Crystalline Lasers : Physical Processes and Operating Schemes*. (1996). doi:10.1109/ACCESS.2015.2424273.

41. Marciniak, L., Strek, W., Bednarkiewicz, A., Lukowiak, A. & Hreniak, D. Bright upconversion emission of Nd3+ in LiLa1-xNdxP4O12 nanocrystalline powders. *Opt Mater (Amst)* **33**, 1492–1494 (2011).

42. Trejgis, K., Lisiecki, R., Bednarkiewicz, A. & Marciniak, L. Nd3+ doped TZPN glasses for NIR operating single band ratiometric approach of contactless temperature readout. *J Lumin* **224**, 117295 (2020).

43. Lenth, W. & Macfarlane, R. M. Excitation mechanisms for upconversion lasers. *J Lumin* **45**, 346–350 (1990).

44. Chadeyron, G. *et al.* Violet upconverted luminescence via photon-avalanche pumping in monoclinic LiKYF5:Nd3+ single-centered laser crystals. *Physica Status Solidi A Appl Res* **171**, 597–604 (1999).

45. Strek, W., Marciniak, L., Hreniak, D. & Lukowiak, A. Anti-Stokes bright yellowish emission of NdAlO3 nanocrystals. *J Appl Phys* **111**, 024305 (2012).

46. Bednarkiewicz, A. & Strek, W. Laser-induced hot emission in Nd 3 /Yb 3 : YAG nanocrystallite ceramics. *J Phys D Appl Phys* **35**, 2503–2507 (2002).

47. Santos, E. P. *et al.* Temperature triggering a photon-avalanche-like mechanism in NdAl3(BO3)4 particles under excitation at 1064 nm. *J Lumin* **245**, 118645 (2022).

48. da Silva, J. F., da Silva, R. F., Santos, E. P., Maia, L. J. Q. & Moura, A. L. Photon-avalanche-like upconversion in NdAl3(BO3)4 nanoparticles excited at 1064 nm. *Appl Phys Lett* **117**, 151102 (2020).

49. Wawrzynczyk, D., Bednarkiewicz, A., Nyk, M., Strek, W. & Samoc, M. Neodymium(iii) doped fluoride nanoparticles as non-contact optical temperature sensors. *Nanoscale* **4**, 6959–6961 (2012).

50. Liu, T.-M. T. M., Conde, J., Lipiński, T., Bednarkiewicz, A. & Huang, C.-C. C. C. Smart NIR linear and nonlinear optical nanomaterials for cancer theranostics: Prospects in photomedicine. *Prog Mater Sci* **88**, 89–135 (2017).

51. Liu, T.-M. T. M., Conde, J., Lipiński, T., Bednarkiewicz, A. & Huang, C.-C. C. C. Revisiting the classification of NIR-absorbing/emitting nanomaterials for in vivo bioapplications. *NPG Asia Mater* **8**, 1–25 (2016).

52. Bednarkiewicz, A., Chan, E. M.-Y., Kotulska, A. M., Marciniak, L. & Prorok, K. Photon avalanche in lanthanide doped nanoparticles for biomedical applications: super-resolution imaging. *Nanoscale Horiz* 1–9 (2019) doi:10.1039/C9NH00089E.

53. Trejgis, K., Maciejewska, K., Bednarkiewicz, A. & Marciniak, L. Near-Infrared-to-Near-Infrared Excited-State Absorption in LaPO4:Nd3+Nanoparticles for Luminescent Nanothermometry. *ACS Appl Nano Mater* **3**, 4818–4825 (2020).

54. Trejgis, K., Tian, F., Li, J., Bednarkiewicz, A. & Marciniak, L. The role of surface related quenching in the single band ratiometric approach based on excited state absorption processes in Nd3+ doped phosphors. *Mater Res Bull* **139**, 111288 (2021).

55. Marciniak, L., Bednarkiewicz, A. & Elzbieciak, K. NIR–NIR photon avalanche based luminescent thermometry with Nd $^{3+}$ doped nanoparticles. *J Mater Chem C Mater* (2018) doi:10.1039/C8TC01553H.

56. Chadeyron, G. *et al.* Violet Upconverted Luminescence via Photon-Avalanche Pumping in Monoclinic LiKYF 5 :Nd 3+ Single-Centered Laser Crystals. *phys. stat. sol. (a)* **171**, (1999).

57. Lenth, W. & Macfarlane, R. M. M. Excitation mechanisms for upconversion lasers. *J Lumin* **45**, 346–350 (1990).

58. Bednarkiewicz, A., Hreniak, D., Dereń, P. & Strek, W. Hot emission in Nd3+/Yb3+:YAG nanocrystalline ceramics. *J Lumin* **102–103**, 438–444 (2003).

59. Bednarkiewicz, A. & Strek, W. Laser-induced hot emission in Nd3+/Yb3+: YAG nanocrystallite ceramics. *J Phys D Appl Phys* **35**, 2503–2507 (2002).

60. Bednarkiewicz, A., Chan, E. M.-Y. E. M. E. M., Kotulska, A. M., Marciniak, L. & Prorok, K. Photon avalanche in lanthanide doped nanoparticles for biomedical applications: super-resolution imaging. *Nanoscale Horiz* **4**, 881–889 (2019).

61. Krasutsky, N. J. 10-μm samarium based quantum counter. *J Appl Phys* **54**, 1261–1267 (1983).

62. Zhu, Y. *et al.* Observation of upconversion white light and ultrabroad infrared emission in YbAG:Ln3+ (Ln = Nd, Sm, Tb, Er). *Applied Physics Express* **8**, 72602 (2015).

63. Luxbacher, T., Fritzer, H. P. & Flint, C. D. Cross relaxation and energy transfer in Cs2NaSmxEuyY1-x-yCl6. *Acta Phys Pol A* **90**, 161–168 (1996).

64. Alvarez-Ramos, M. E. Luminescence and study of channels for cross-relaxation dependent on the concentration of Sm3+ under simultaneous UV-IR excitation in tellurite-germanate glasses. *J Alloys Compd* **854**, 157076 (2021).

65. Ahmadi, F., Hussin, R. & Ghoshal, S. K. Judd-Ofelt intensity parameters of samarium-doped magnesium zinc sulfophosphate glass. *J Non Cryst Solids* **448**, 43–51 (2016).

66. Drabik, J., Kowalski, R. & Marciniak, L. Enhancement of the sensitivity of single band ratiometric luminescent nanothermometers based on Tb3+ ions through activation of the cross relaxation process. *Sci Rep* **10**, 1–11 (2020).

67. Drabik, J. & Marciniak, L. KLaP4O12:Tb3+ Nanocrystals for Luminescent Thermometry in a Single-Band-Ratiometric Approach. *ACS Appl Nano Mater* **3**, 3798–3806 (2020).

68. Drabik, J., Ledwa, K. & Marciniak, Ł. Implementing Defects for Ratiometric Luminescence Thermometry. *Nanomaterials* **10**, 1333 (2020).

69. Drabik, J. & Marciniak, L. Excited State Absorption for Ratiometric Thermal Imaging. *ACS Appl Mater Interfaces* acsami.0c18570 (2020) doi:10.1021/acsami.0c18570.

70. Optical spectroscopy of Dy3+-doped CaGdAlO4 single crystal for potential use in solid-state yellow lasers | Elsevier Enhanced Reader.

71. Malinowski, M. *et al.* Spectroscopy and upconversion processes in YAlO3:Ho3+ crystals. *Opt Mater (Amst)* **12**, 409–423 (1999).

72. Liu, G. K., Chen, Y. H. & Beitz, J. v. Photon avalanche up-conversion in Ho > doped fluoride glasses. **81**, 7–12 (1999).

73. Babu, P. *et al.* Photon avalanche upconversion in Ho3+-Yb3+ co-doped transparent oxyfluoride glass-ceramics. *Chem Phys Lett* **600**, 34–37 (2014).

74. Luo, X. xian & Cao, W. he. Upconversion luminescence of holmium and ytterbium co-doped yttrium oxysulfide phosphor. *Mater Lett* **61**, 3696–3700 (2007).

75. Dang, S. *et al.* Near-infrared luminescence from sol-gel materials doped with holmium(III) and thulium(III) complexes. *Journal of Physical Chemistry C* **112**, 13240–13247 (2008).

76. Shcherbakov, I. A., Klimov, L. v. & Tsvetkov, V. B. Room Temperature 2-µm Laser Action of Ho3+-Doped YSGG, GSAG, YSAG, and YAG Crystals. *Advanced Solid State Lasers (1993), paper ML7* ML7 (1993) doi:10.1364/ASSL.1993.ML7.

77. Kalisky, Y., Rotman, S. R., Boulon, G., Pedrini, C. & Brenier, A. Spectroscopy, Modelling and Laser Operation of Holmium Doped Laser Crystals. *MRS Online Proceedings Library 1993 329:1* **329**, 121–129 (1993).

78. Antipenko, B. M. *et al.* Periodic-pulse operation of holmium lasers using YAG and YSGG crystals. *Quantum Elec (Woodbury)* **23**, 997–998 (1993).

79. Kampantais, S. *et al.* Assessing the Learning Curve of Holmium Laser Enucleation of Prostate (HoLEP). A Systematic Review. *Urology* **120**, 9–22 (2018).

80. Gan, F., Wang, J. & Chen, Y. Nonlinear luminescence of and ions in ZBLAN fluoride glasses. *Pure and Applied Optics: Journal of the European Optical Society Part A* **5**, 855 (1996).

81. Malinowski, M. *et al.* Spectroscopy and upconversion processes in YAlO3:Ho3+ crystals. *Opt Mater (Amst)* **12**, 409–423 (1999).

82. Liu, O. K., Chen, Y. H. & Beitz, J. V. Photon avalanche up-conversion in Ho3+ doped fluoride glasses. *J Lumin* **81**, 7–12 (1999).

83. Alimov, O. K. *et al.* Nonlinear luminescence of and ions in ZBLAN fluoride glasses. *Pure and Applied Optics: Journal of the European Optical Society Part A* **5**, 855 (1996).

84. Brenier, A., Garapon, C., Madej, C., Pédrini, C. & Boulon, G. Dynamics of looping mechanisms in laser crystals. *Opt Mater (Amst)* **4**, 51–54 (1994).

85. Malinowski, M. *et al.* Room temperature photon avalanche in Ho3+ doped YAG, YAP, YLF and ZBLAN. *J Alloys Compd* **323–324**, 731–735 (2001).

86. Kuck, S. & Sokólska, I. The up-conversion of near-infrared excitation radiation in Ho3+-doped LiYF4. *Chem Phys Lett* **325**, 257–263 (2000).

87. Lahoz, F., Martín, I. R. & Calvilla-Quintero, J. M. Ultraviolet and white photon avalanche upconversion in Ho3+-doped nanophase glass ceramics. *Appl Phys Lett* **86**, 051106 (2005).

88. Lahoz, F. *et al.* Room temperature photon avalanche up-conversion in Ho3+ doped fluoroindate glasses under excitation at 747 nm. *Opt Mater (Amst)* **25**, 209–213 (2004).

89. Wnuk, A. *et al.* Infra-red to visible up-conversion in holmium-doped materials. *J Alloys Compd* **341**, 353–357 (2002).

90. Lahoz, F., Martín, I. R. & Briones, A. Infrared-laser induced photon avalanche upconversion in Ho3+–Yb3+ codoped fluoroindate glasses. *J Appl Phys* **95**, 2957 (2004).

91. Osiac, E., Sokólska, I. & Kück, S. Avalanche-like mechanisms and up-conversion processes under infrared pumping in Ho3+, Yb3+:YAlO3. *J Lumin* **94–95**, 289–292 (2001).

92. Dwivedi, Y., Bahadur, A. & Rai, S. B. Optical avalanche in Ho:Yb:Gd2O3 nanocrystals. *J Appl Phys* **110**, 043103 (2011).

93. Dwivedi, Y., Bahadur, A. & Rai, S. B. Optical avalanche in Ho : Yb : Gd2O3 nanocrystals. **043103**, (2016).

94. Dong, H. *et al.* Lanthanide Nanoparticles: From Design toward Bioimaging and Therapy. *Chem Rev* **115**, 10725–10815 (2015).

95. Zheng, B. *et al.* Rare-Earth Doping in Nanostructured Inorganic Materials. *Chem Rev* **122**, 5519–5603 (2022).

96. Auzel, F. & Chen, Y. Photon avalanche luminescence of Er3+ ions in LiYF4 crystal. *J Lumin* **65**, 45–56 (1995).

97. Auzel, F. & Chen, Y. H. Multiphonon pumping in Er3+ ZBLAN bulk and fibre, the first step for the photon avalanche process. *J Non Cryst Solids* **184**, 57–60 (1995).

98. Chen, Y., Auzel, F. & Chen, Y. Spatial domains in avalanche pumped Er:ZBLAN fibre. *Electron Lett* **30**, 323–324 (1994).

99. Chent, Y., Meichenint, D. & Auzelt, F. Room-temperature photon avalanche up-conversion in Er-doped fluoride glass and fibre pumped at 700 nm. *J. Phys.: Condens. Matter* **7**, 3363–3370 (1995).

100. Chen, Y. & Auzel, F. Room-temperature photon avalanche up-conversion in an erbium-doped fluoride fibre. *J Phys D Appl Phys* **28**, 207 (1995).

101. Singh, A. K. *et al.* Photon avalanche upconversion and pump power studies in LaF3:Er3+/Yb3+phosphor. *Appl Phys B* **104**, 1035–1041 (2011).

102. Chent, Y., Meichenint, D. & Auzelt, F. Room-temperature photon avalanche up-conversion in Er-doped fluoride glass and fibre pumped at 700 nm. *J. Phys.: Condens. Matter* **7**, 3363–3370 (1995).

103. Hebert, T., Wannemacher, R., MacFarlane, R. M. & Lenth, W. Blue continuously pumped upconversion lasing in Tm:YLiF4. *Appl Phys Lett* **60**, 2592–2594 (1992).

104. Ni, H. & Rand, S. C. Avalanche upconversion in Tm:YALO_3. *Opt Lett* **16**, 1424 (1991).

105. Guy, S., Joubert, M. F. & Jacquier, B. Photon avalanche upconversion in various Tm3+-doped materials. *J Alloys Compd* **275–277**, 186–190 (1998).

106. Bielejec, E., Kisel, E. & Silversmith, A. Red to blue up-conversion in Y2SiO5:Tm3+. *J Lumin* **72–74**, 62–64 (1997).

107. Joubert, M. F., Guy, S., Linarès, C., Jacquier, B. & Adam, J. L. Avalanche upconversion in Tm3+-doped BIGaZYTZr glass. *J Non Cryst Solids* **184**, 98–102 (1995).

108. Martín, I. R. *et al.* Room-temperature photon avalanche upconversion in Tm3+: Y2O3 crystals. *Phys Rev B* **60**, 7252–7257 (1999).

109. Guy, S., Shepherd, D. P., Joubert, M. F., Jacquier, B. & Poignant, H. Blue avalanche upconversion in Tm:ZBLAN fiber. *Journal of the Optical Society of America B* **14**, 926 (1997).

110. Dyson, J. M. *et al.* Observation of avalanche-like behavior in Tm3+ : Y2O3. *J Lumin* **60–61**, 668–671 (1994).

111. Martín, I. R. *et al.* Room temperature photon avalanche upconversion in Tm3+-doped fluoroindate glasses. *Journal of Physics Condensed Matter* **12**, 1507–1516 (2000).

112. Martín, I. R. *et al.* Room temperature photon avalanche upconversion in Tm3+-doped fluoroindate glasses. *Journal of Physics Condensed Matter* **12**, 1507–1516 (2000).

113. Martín, I. R. *et al.* Room-temperature photon avalanche upconversion in Tm3+: Y2O3 crystals. *Phys Rev B* **60**, 7252–7257 (1999).

114. Hebert, T., Wannemacher, R., MacFarlane, R. M. M. & Lenth, W. Blue continuously pumped upconversion lasing in Tm:YLiF4. *Appl Phys Lett* **60**, 2592–2594 (1992).

115. Ni, H. & Rand, S. C. Avalanche upconversion in Tm:YALO_3. *Opt Lett* **16**, 1424 (1991).

116. Guy, S., Joubert, M. F. & Jacquier, B. Photon avalanche upconversion in various Tm3+-doped materials. *J Alloys Compd* **275–277**, 186–190 (1998).

117. Dyson, J. M. *et al.* Observation of avalanche-like behavior in Tm3+ : Y2O3. *J Lumin* **60–61**, 668–671 (1994).

118. Bielejec, E., Kisel, E. & Silversmith, A. Red to blue up-conversion in Y2SiO5 Tm3+. *J.Luminescence* **72–74**, 62–64 (1997).

119. Guy, S., Joubert, M. F. & Jacquier, B. The photon avalanche as a bifurcation phenomenon Application to various Tm3+ doped materials. *J.Luminescence* **72–74**, 65–67 (1997).

120. Guy, S., Shepherd, D. P., Joubert, M. F., Jacquier, B. & Poignant, H. Blue avalanche upconversion in Tm:ZBLAN fiber. *Journal of the Optical Society of America B* **14**, 926 (1997).

121. Lee, C. *et al.* Giant nonlinear optical responses from photon avalanching nanoparticles. (2020).

122. Plöschner, M. *et al.* Simultaneous super-linear excitation-emission and emission depletion allows imaging of upconversion nanoparticles with higher sub-diffraction resolution. *Opt Express* **28**, 24308 (2020).

123. Liu, Y. *et al.* Amplified stimulated emission in upconversion nanoparticles for super-resolution nanoscopy. *Nature* **543**, 229–233 (2017).

124. Dudek, M. *et al.* Size-Dependent Photon Avalanching in Tm3+ Doped LiYF4 Nano, Micro, and Bulk Crystals. *Adv Opt Mater* 2201052 (2022) doi:10.1002/ADOM.202201052.

125. Villanueva-Delgado, P., Biner, D. & Krämer, K. W. Judd–Ofelt analysis of β-NaGdF4: Yb3+, Tm3+ and β-NaGdF4:Er3+ single crystals. *J Lumin* **189**, 84–90 (2017).

126. Strz, A., Szatko, M., Potrz, K. & Ryba-romanowski, W. single crystals. **220**, (2020).

127. Jia, Z. *et al.* Enhancement of 800 nm upconversion emission in a thulium doped tellurite microstructured fiber pumped by a 1560 nm femtosecond fiber laser. *J Appl Phys* **119**, (2016).

128. Balda, R. *et al.* Spectroscopic properties of the 1.4 µm emission of Tm^3+ ions in TeO_2-WO_3-PbO glasses. *Opt Express* **16**, 11836 (2008).

129. Deng, H. *et al.* Additive-mediated splitting of lanthanide orthovanadate nanocrystals in water: Morphological evolution from rods to sheaves and to spherulites. *Cryst Growth Des* **8**, 4432–4439 (2008).

130. Deng, H., Yang, S., Xiao, S., Gong, H. M. & Wang, Q. Q. Controlled synthesis and upconverted avalanche luminescence of cerium(III) and neodymium(III) orthovanadate nanocrystals with high uniformity of size and shape. *J Am Chem Soc* **130**, 2032–2040 (2008).

131. Joshi, C. & Rai, S. B. Structural, thermal, and optical properties of Pr 3+/Yb 3+ co-doped oxyhalide tellurite glasses and its nano-crystalline parts. *Solid State Sci* **14**, 997–1003 (2012).

132. Chivian, J. S., Case, W. E. & Eden, D. D. Cite as. *Luminescence in Solids The Journal of Chemical Physics* **35**, 836 (1979).

133. Zhu, Z. *et al.* Three-dimensional, dual-color nanoscopy enabled by migrating photon avalanches with one single low-power CW beam. *Sci Bull (Beijing)* **69**, 458–465 (2023).

134. Dudek, M. *et al.* Understanding Yb $^{3+}$ -sensitized photon avalanche in Pr $^{3+}$ co-doped nanocrystals: modelling and optimization. *Nanoscale* **15**, 18613–18623 (2023).

135. Bednarkiewicz, A. & Strek, W. Laser-induced hot emission in Nd 3 /Yb 3 : YAG nanocrystallite ceramics. *J Phys D Appl Phys* **35**, 2503–2507 (2002).

136. Xiao, S., Zhou, L., Wang, Q. Q., Deng, H. & Yang, S. H. Energy transfer and avalanche upconversion of ndxy1-xvo4nanocrystals. *Chinese Physics Letters* **26**, 1–5 (2009).

137. Da Silva, J. F., Da Silva, R. F., Santos, E. P., Maia, L. J. Q. & Moura, A. L. Photon-avalanche-like upconversion in NdAl3(BO3)4nanoparticles excited at 1064 nm. *Appl Phys Lett* **117**, 151102 (2020).

138. Zhang, Z. *et al.* Tuning Phonon Energies in Lanthanide-doped Potassium Lead Halide Nanocrystals for Enhanced Nonlinearity and Upconversion. *Angewandte Chemie - International Edition* **62**, e202212549 (2023).

139. Skripka, A. *et al.* Intrinsic Optical Bistability of Photon Avalanching Nanocrystals. http://arxiv.org/abs/2403.04098 (2024).

140. Zhu, Y. *et al.* Observation of upconversion white light and ultrabroad infrared emission in YbAG:Ln^{3+} (Ln = Nd, Sm, Tb, Er). *Applied Physics Express* **8**, 3–7 (2015).

141. Skripka, A. *et al.* A Generalized Approach to Photon Avalanche Upconversion in Luminescent Nanocrystals. *Nano Lett* **23**, 7100–7106 (2023).

142. Babu, P. *et al.* Photon avalanche upconversion in Ho3+-Yb3+ co-doped transparent oxyfluoride glass-ceramics. *Chem Phys Lett* **600**, 34–37 (2014).

143. Rathaiah, M. *et al.* Photon avalanche upconversion in Ho3+-doped gallium nano-garnets. *Opt Mater (Amst)* **39**, 16–20 (2015).

144. Dwivedi, Y., Bahadur, A. & Rai, S. B. Optical avalanche in Ho : Yb : Gd2O3 nanocrystals. **043103**, (2016).

145. Wang, C. *et al.* Tandem Photon Avalanches for Various Nanoscale Emitters with Optical Nonlinearity up to 41st-Order through Interfacial Energy Transfer. *Advanced Materials* **2**, e2307848 (2023).

146. Joshi, C., Rai, R. N. & Rai, S. B. Structural, thermal, and optical properties of Er 3+/Yb 3+ co-doped oxyhalide tellurite glasses, glass-ceramics and ceramics. *J Quant Spectrosc Radiat Transf* **113**, 397–404 (2012).

147. Marciniak, L., Stefanski, M., Tomala, R., Hreniak, D. & Strek, W. Synthesis and up-conversion luminescence of Er3+ and Y b3+ codoped nanocrystalline tetra- (KLaP4O12) and pentaphosphates (LaP5O14). *Journal of Chemical Physics* **143**, (2015).

148. Kumar, A. & Bahadur, A. Intense green upconversion emission by photon avalanche process from Er3+/Yb3+ co-doped NaBi(WO4)2 phosphor. *J Alloys Compd* **857**, 158196 (2021).

149. Bian, W. *et al.* Controllable synergistic effect of Yb3+, Er3+ co-doped KLu2F7 with the assistant of defect state. *CrystEngComm* **18**, 2642–2649 (2016).

150. Li, Y. *et al.* Unusually enhancing high-order photon avalanche upconversion of layered BiOCl: Er3+semiconductor poly-crystals via Li+ion intercalation doping. *Mater Des* **105**, 290–295 (2016).

151. Wang, F., Yang, B., Yu, Q., Liu, D. & Ma, W. Cooperative upconversion luminescence of Er3 + in Gd2O3 − xSx phosphor. *Spectrochim Acta A Mol Biomol Spectrosc* **190**, 312–317 (2018).

152. Li, Y. *et al.* BiOCl:Er3+ Nanosheets with Tunable Thickness for Photon Avalanche Phosphors. *Cite This: ACS Appl. Nano Mater* **13**, (2019).

153. Xiao, T. *et al.* Modification photon avalanche emission of BiOCl: Er3+ nanosheets through facile solvent-thermal synthesis. *Inorg Chem Commun* **117**, 107934 (2020).

154. Xiao, T. *et al.* Multi-photon near-infrared emission of Er3+ ions induced by upconversion self-sensitization of layered polarized Bi9V2O18Cl semiconductor with narrow-band. *J Lumin* **232**, 117819 (2021).

155. Levy, E. S. *et al.* Energy-Looping Nanoparticles: Harnessing Excited-State Absorption for Deep-Tissue Imaging. *ACS Nano* **10**, 8423–8433 (2016).

156. Lee, C. *et al.* Indefinite and Bidirectional Near Infrared Nanocrystal Photoswitching. *Nature* **618**, 951–958 (2023).

157. Levy, E. S. *et al.* Energy-Looping Nanoparticles: Harnessing Excited-State Absorption for Deep-Tissue Imaging. *ACS Nano* **10**, 8423–8433 (2016).

158. Denkova, D. *et al.* 3D sub-diffraction imaging in a conventional confocal configuration by exploiting super-linear emitters. *Nat Commun* 1–12 (2019) doi:10.1038/s41467-019-11603-0.

159. Liu, Y. *et al.* Controlled Assembly of Upconverting Nanoparticles for Low-Threshold Microlasers and Their Imaging in Scattering Media. *ACS Nano* acsnano.9b06102 (2020) doi:10.1021/acsnano.9b06102.

160. Liu, B. *et al.* Upconversion Nonlinear Structured Illumination Microscopy. (2020) doi:10.1021/acs.nanolett.0c00448.

161. Lee, C. *et al.* Giant nonlinear optical responses from photon-avalanching nanoparticles. *Nature* **589**, 230–235 (2021).

162. Zhang, M. *et al.* Lanthanide-Doped KMgF $_3$ Upconversion Nanoparticles for Photon Avalanche Luminescence with Giant Nonlinearities. *Nano Lett* **23**, 8576–8584 (2023).

163. Zheng, W. *et al.* Warm white broadband emission and tunable long lifetimes in Yb3+ doped Gd2O3 nanoparticles. *Ceram Int* **46**, 22900–22906 (2020).

164. Kolesov, R. *et al.* Super-resolution upconversion microscopy of praseodymium-doped yttrium aluminum garnet nanoparticles. *Phys. Rev. B* **84**, (2011).

165. Caillat, L. *et al.* Multiphoton upconversion in rare earth doped nanocrystals for sub-diffractive microscopy. *Appl Phys Lett* **102**, 143114 (2013).

166. Wang, B. *et al.* Visible-to-visible four-photon ultrahigh resolution microscopic imaging with 730-nm diode laser excited nanocrystals. *Opt Express* **24**, A302 (2016).

167. Mi, Z. *et al.* Subwavelength imaging through ion-beam-induced upconversion. *Nat Commun* **6**, 1–6 (2015).

168. Wu, Q., Huang, B., Peng, X., He, S. & Zhan, Q. Non-bleaching fluorescence emission difference microscopy using single 808-nm laser excited red upconversion emission. *Opt Express* **25**, 30885 (2017).

169. Zhan, Q. *et al.* Achieving high-efficiency emission depletion nanoscopy by employing cross relaxation in upconversion nanoparticles. *Nat Commun* **8**, 1058 (2017).

170. Chen, C. *et al.* Multi-photon near-infrared emission saturation nanoscopy using upconversion nanoparticles. *Nat Commun* **9**, (2018).

171. Peng, X. *et al.* Fast upconversion super-resolution microscopy with 10 µs per pixel dwell times. *Nanoscale* **11**, 1563–1569 (2019).

172. Krause, S., Liisberg, M. B., Lahtinen, S., Soukka, T. & Vosch, T. Lanthanide-Doped Nanoparticles for Stimulated Emission Depletion Nanoscopy. *ACS Appl Nano Mater* **2**, 5817–5823 (2019).

173. Liu, Y. *et al.* Super-Resolution Mapping of Single Nanoparticles inside Tumor Spheroids. (2020) doi:10.1002/smll.201905572.

174. Liu, B., Chen, C., Liao, J. & Wen, S. Upconversion nonlinear structured illumination microscopy. (2020).

175. Wu, H. *et al.* Versatile cascade migrating photon avalanches for full-spectrum extremely nonlinear emissions and super-resolution microscopy. *Advanced Photonics* **6**, (2024).